Available online at www.sciencedirect.com
ScienceDirect
Journal of Computational Physics 225 (2007) 1508–1532
JOURNAL OF COMPUTATIONAL PHYSICS
www.elsevier.com/locate/jcp

Outflow boundary conditions for the Fourier transformed three-dimensional Vlasov–Maxwell system

B. Eliasson

Department of Physics, Umeå University, SE-901 87 Umeå, Sweden
Theoretische Physik IV, Ruhr-Universität Bochum, D-44780 Bochum, Germany

Received 26 October 2006; received in revised form 27 January 2007; accepted 1 February 2007
Available online 17 February 2007

Abstract

A problem with the solution of the Vlasov equation is its tendency to become filamented/oscillatory in velocity space, which in numerical simulations can give rise to unphysical oscillations and recurrence effects. We present a three-dimensional Vlasov–Maxwell solver (three spatial and velocity dimensions, plus time), in which the Vlasov equation is Fourier transformed in velocity space and the resulting equations solved numerically. By designing absorbing outflow boundary conditions in the Fourier transformed velocity space, the highest Fourier modes in velocity space are removed from the numerical solution. This introduces a dissipative effect in velocity space and the numerical recurrence effect is strongly reduced. The well-posedness of the boundary conditions is proved analytically, while the stability of the numerical implementation is assessed by long-time numerical simulations. Well-known wave-modes in magnetized plasmas are shown to be reproduced by the numerical scheme.

Keywords: Vlasov–Maxwell system; Fourier method; Outflow boundary

1. Introduction

The most common method to solve the Vlasov equation is with the particle-in-cell (PIC) method [1,2]. In this method, the Vlasov equation is solved by following the trajectories of a set of statistically distributed super-particles, which resolves the particle distribution functions in phase space. Each super-particle represents a large number of real particles. PIC simulations have proven to be extremely successful due to their relative simplicity and adaptivity, especially in problems involving large-amplitude waves and beams. However, the statistical noise of PIC simulations sometimes overshadows the physical results, and for some problems, the low-density velocity tail of the particle distribution cannot be resolved with high enough accuracy by the super-particles.

As a contrast, grid-based Vlasov solvers discretizes the particle distribution function directly in the form of a phase fluid which is represented on a grid in both space and velocity (or momentum) space. The advantage

E-mail address: bengt@tp4.ruhr-uni-bochum.de

0021-9991/$ - see front matter
doi:10.1016/j.jcp.2007.02.005

with grid-based Vlasov solvers is that there is no statistical noise in the simulations, and that the dynamical range is determined by the number system of the computer rather than super particles. Hence the low-density velocity tail of the particle distribution can be resolved much more accurately by grid-based Vlasov solvers, which makes them suitable for certain types of problems. A disadvantage with grid-based Vlasov solvers in higher dimensions is that the full phase-space has to be discretized on a grid, which makes both the storage of the data in the computer's memory, and the numerical calculations, extremely demanding. These problems are today treated most efficiently by well known PIC codes by enhancing the number of macro-particles. Another problem is the tendency of the distribution function to become oscillatory in velocity space, leading to unphysical noise and recurrence effects in the numerical solution. This was recognized in early Vlasov simulations [3] and special methods were devised to resolve this problem, for example in the time-spitting method [4,5] where a smoothing operator was applied to remove the highest oscillations in velocity space. The time-splitting method has been extended to multiple dimensional Vlasov–Maxwell system where a Van Leer type of dissipative scheme was used [6]. A scheme based on finite volume conservative discretization has also been developed [7], in which an upwind scheme with second-order flux limiter was used to reduce unphysical oscillations in velocity space. A back-substitution method, which avoids artificial heating of the plasmas, has been designed for the integration of the Vlasov equation in a magnetic field [8]. Several Eulerian grid-based solvers are reviewed and compared in Refs. [9,10]. For the Fourier-Fourier method, in which the Vlasov equation is Fourier transformed in both configuration space and velocity space, a filtered method was developed based on a convolution by a Gaussian function in velocity space [11,12], leading to a smoother solution. The Fourier transformed Vlasov equation was also studied both theoretically and numerically to give a new interpretation of Landau damping, the time echo phenomenon etc., in terms of imperfectly trapped (leaking) waves in the Fourier transformed velocity space [13,14]. For methods using Hermite polynomials to resolve the velocity space, methods have been developed in which the highest-order Hermite polynomials absorb the oscillations in velocity space [15,16], thereby reducing numerical recurrence effects strongly. For the Fourier method in one and two dimensions [17–19], absorbing boundary conditions were designed at the largest Fourier mode in velocity space so that the highest oscillations in velocity space were removed from the solution. In this manner, the recurrence effect could be strongly reduced, compared to the naive method of setting the highest Fourier component to zero.

In this article, we extend the algorithms for solving the Fourier transformed one- and two-dimensional Vlasov–Maxwell system [17–19] to three velocity and spatial dimensions, plus time. The absorbing boundary conditions for the Vlasov equation in the Fourier transformed velocity space is proved to be well-posed, and we demonstrate by long simulations with random numbers as initial conditions that there are no numerical instabilities in the system. Several simulations are performed to assess that the numerical scheme reproduces known wave modes in magnetized plasmas.

The article is organized in the following fashion. In Section 2 the three-dimensional Vlasov–Maxwell system is discussed, together with the Fourier transform technique in velocity space. Well-posed boundary conditions are derived in preparation for the numerical simulation of the Fourier-transformed system. The numerical schemes used to approximate the time-dependent solution of the Vlasov equation system are described in Section 3, and the numerical experiments and results are presented in Section 4, where the results are compared with known theory. In Section 5 some conclusions are drawn and future perspectives discussed.

2. The Vlasov–Maxwell system

The Vlasov equation

$$\frac{\partial f_\alpha}{\partial t} + \mathbf{v}\cdot\nabla_{\mathbf{x}} f_\alpha + \frac{q_\alpha}{m_\alpha}(\mathbf{E}+\mathbf{v}\times\mathbf{B})\cdot\nabla_{\mathbf{v}} f_\alpha = 0, \tag{1}$$

describes the evolution of the distribution function $f_\alpha(\mathbf{x},\mathbf{v},t)$ of electrically charged particles of type α (here α equals i for ions and e for electrons) in the presence of the electric and magnetic field $\mathbf{E}$ and $\mathbf{B}$, respectively, each particle having the electric charge q_α and mass m_α. One Vlasov equation is needed for each species of particles. Below, we will assume electrons and one species of singly charged ions so that $q_e = -e$ and $q_i = -e$ where e is the magnitude of the electron charge.

The charge and current densities act as sources of self-consistent electromagnetic fields governed by the Maxwell equations

$$\nabla_{\mathbf{x}} \cdot \mathbf{E} = \frac{\rho}{\varepsilon_0}, \quad \nabla_{\mathbf{x}} \cdot \mathbf{B} = 0, \tag{2}$$

$$\nabla_{\mathbf{x}} \times \mathbf{E} = -\frac{\partial \mathbf{B}}{\partial t}, \quad \nabla_{\mathbf{x}} \times \mathbf{B} = \mu_0 \mathbf{j} + \frac{1}{c^2}\frac{\partial \mathbf{E}}{\partial t}, \tag{3}$$

where μ_0 is the vacuum permeability, ε_0 is the vacuum permittivity and $c = 1/\sqrt{\mu_0 \varepsilon_0}$ is the speed of light in vacuum. The charge and current densities ρ and $\mathbf{j}$ are defined as

$$\rho = \sum_\alpha q_\alpha n_\alpha, \quad \mathbf{j} = \sum_\alpha q_\alpha n_\alpha \mathbf{v}_\alpha, \tag{4}$$

and where the particle number densities $n_\alpha(\mathbf{x}, t)$ and mean velocities $\mathbf{v}_\alpha(\mathbf{x}, t)$ are obtained as moments of the distribution function as

$$n_\alpha = \int_{-\infty}^{\infty} f_\alpha(\mathbf{x}, \mathbf{v}, t) \mathrm{d}^3 v, \quad \mathbf{v}_\alpha = \frac{1}{n_\alpha}\int_{-\infty}^{\infty} \mathbf{v} f_\alpha(\mathbf{x}, \mathbf{v}, t) \mathrm{d}^3 v, \tag{5}$$

respectively. In our treatment, the electric and magnetic fields are given in terms of the electrodynamic scalar and vector potentials as

$$\mathbf{E} = -\nabla_{\mathbf{x}} \Phi - \frac{\partial \mathbf{A}}{\partial t}, \tag{6}$$

and

$$\mathbf{B} = \mathbf{B}_0 + \nabla_{\mathbf{x}} \times \mathbf{A}, \tag{7}$$

where $\mathbf{B}_0$ is the external magnetic field. Using the Lorentz condition

$$\nabla_{\mathbf{x}} \cdot \mathbf{A} + \frac{1}{c^2}\frac{\partial \phi}{\partial t} = 0, \tag{8}$$

the scalar and vector potentials follow the Lorentz wave equations

$$\frac{1}{c^2}\frac{\partial \Phi}{\partial t^2} - \nabla_{\mathbf{x}}^2 \Phi = \frac{\rho}{\varepsilon_0}, \tag{9}$$

$$\frac{1}{c^2}\frac{\partial^2 \mathbf{A}}{\partial t^2} - \nabla_{\mathbf{x}}^2 \mathbf{A} = \mu_0 \mathbf{j}. \tag{10}$$

Instead of using directly Eq. (9), we will use the first of Maxwell's equations (2) and the definition (6) of the electric field to obtain

$$\frac{\rho}{\varepsilon_0} = \nabla_{\mathbf{x}} \cdot \mathbf{E} = -\nabla_{\mathbf{x}}^2 \Phi - \nabla_{\mathbf{x}} \cdot \frac{\partial \mathbf{A}}{\partial t} \tag{11}$$

or

$$-\nabla_{\mathbf{x}}^2 \Phi = \frac{\rho}{\varepsilon_0} + \nabla_{\mathbf{x}} \cdot \frac{\partial \mathbf{A}}{\partial t}. \tag{12}$$

By introducing a new variable $\mathbf{\Gamma}$ for the time-derivative of $\mathbf{A}$, Eqs. (10) and (12) can be written as a first-order system of equations with respect to time,

$$\frac{\partial \mathbf{A}}{\partial t} = \mathbf{\Gamma}, \qquad \frac{\partial \mathbf{\Gamma}}{\partial t} = c^2(\nabla_{\mathbf{x}}^2 \mathbf{A} + \mu_0 \mathbf{j}), \tag{13}$$

$$-\nabla_{\mathbf{x}}^2 \phi = \frac{\rho}{\varepsilon_0} + \nabla_{\mathbf{x}} \cdot \mathbf{\Gamma}, \tag{14}$$

and the electric field (6) is obtained as

$$\mathbf{E} = -\nabla_{\mathbf{x}} \phi - \mathbf{\Gamma}. \tag{15}$$

The Vlasov equations (1) together with the wave equation (13), coupled with Eqs. (7), (14) and (15), form a closed system.

By using the Fourier transform pair

$$f_\alpha(\mathbf{x},\mathbf{v},t) = \int_{-\infty}^{\infty} \hat{f}_\alpha(\mathbf{x},\boldsymbol{\eta},t)\mathrm{e}^{-\mathrm{i}\boldsymbol{\eta}\cdot\mathbf{v}}\mathrm{d}^3\eta, \tag{16}$$

$$\hat{f}_\alpha(\mathbf{x},\boldsymbol{\eta},t) = \frac{1}{(2\pi)^3}\int_{-\infty}^{\infty} f_\alpha(\mathbf{x},\mathbf{v},t)\mathrm{e}^{\mathrm{i}\boldsymbol{\eta}\cdot\mathbf{v}}\mathrm{d}^3v, \tag{17}$$

the velocity variable $\mathbf{v}$ is transformed into a new variable $\boldsymbol{\eta}$ and the unknown function $f(\mathbf{x},\mathbf{v},t)$ is changed to a new, complex valued, function $\hat{f}(\mathbf{x},\boldsymbol{\eta},t)$, which obeys the Fourier transformed Vlasov equation

$$\frac{\partial \hat{f}_\alpha}{\partial t} - \mathrm{i}\nabla_{\mathbf{x}}\cdot\nabla_{\boldsymbol{\eta}}\hat{f}_\alpha - \frac{q_\alpha}{m_\alpha}\{\mathrm{i}\mathbf{E}\cdot\boldsymbol{\eta}\hat{f}_\alpha + \nabla_{\boldsymbol{\eta}}\cdot[(\mathbf{B}\times\boldsymbol{\eta})\hat{f}_\alpha]\} = 0. \tag{18}$$

The nabla operators $\nabla_{\mathbf{x}}$ and $\nabla_{\boldsymbol{\eta}}$ denote differentiation with respect to $\mathbf{x}$ and $\boldsymbol{\eta}$, respectively.

Since f_α is a real-values function, the Fourier transformed function $\hat{f}$ has the symmetry property

$$\hat{f}_\alpha(\mathbf{x},-\boldsymbol{\eta},t) = \hat{f}^*_\alpha(\mathbf{x},\boldsymbol{\eta},t), \tag{19}$$

where the asterisk denotes complex conjugation. This will be used in the numerical procedure to reduce the number of grid points used in $\boldsymbol{\eta}$ space to represent the particle distribution function. We note that the real part of $\hat{f}_\alpha$ is an even function with respect to $\boldsymbol{\eta}$, while the imaginary part of $\hat{f}_\alpha$ is odd with respect to $\boldsymbol{\eta}$.

In the Fourier transformed variables, the particle number densities and mean velocities are obtained as

$$n_\alpha(\mathbf{x},t) = (2\pi)^3\hat{f}_\alpha(\mathbf{x},\eta,t)_{\boldsymbol{\eta}=0} = (2\pi)^3\Re[\hat{f}_\alpha(\mathbf{x},\eta,t)]_{\boldsymbol{\eta}=0} \tag{20}$$

and

$$\mathbf{v}_\alpha(\mathbf{x},t) = -\mathrm{i}\frac{(2\pi)^3}{n_\alpha(\mathbf{x},t)}[\nabla_{\boldsymbol{\eta}}\hat{f}_\alpha(\mathbf{x},\boldsymbol{\eta},t)]_{\boldsymbol{\eta}=0} = \frac{(2\pi)^3}{n_\alpha(\mathbf{x},t)}\{\nabla_{\boldsymbol{\eta}}\Im[\hat{f}_\alpha(\mathbf{x},\boldsymbol{\eta},t)]\}_{\boldsymbol{\eta}=0}, \tag{21}$$

respectively. One can note that the integrals over infinite $\mathbf{v}$ space have been converted to evaluations in $\boldsymbol{\eta}$ space. Here $\Re[\hat{f}_\alpha]$ and $\Im[\hat{f}_\alpha]$ denote the real and imaginary part of $\hat{f}_\alpha$, respectively. The last equalities in Eqs. (20) and (21) follow from the symmetry property (19) at $\boldsymbol{\eta} = 0$.

2.1. Invariants of the Vlasov–Maxwell system

The three-dimensional system (1)–(3) conserves the energy norm

$$\|f_\alpha\|^2 = \int_{\Omega_{\mathbf{x}}}\int_{\Omega_{\mathbf{v}}} f_\alpha^2\mathrm{d}\Omega_{\mathbf{v}}\mathrm{d}\Omega_{\mathbf{x}}, \tag{22}$$

the total number of particles

$$N_\alpha = \int_{\Omega_{\mathbf{x}}}\int_{\Omega_{\mathbf{v}}} f_\alpha\mathrm{d}\Omega_{\mathbf{v}}\mathrm{d}\Omega_{\mathbf{x}}, \tag{23}$$

the total linear momentum

$$\mathbf{p} = \int_{\Omega_{\mathbf{x}}}\left[\int_{\Omega_{\mathbf{v}}}\mathbf{v}(m_i f_i + m_e f_e)\mathrm{d}\Omega_{\mathbf{v}} + \varepsilon_0\mathbf{E}\times\mathbf{B}\right]\mathrm{d}\Omega_{\mathbf{x}} \tag{24}$$

and the total energy

$$W = \int_{\Omega_{\mathbf{x}}}\left[\int_{\Omega_{\mathbf{v}}}\frac{1}{2}\mathbf{v}^2(m_i f_i + m_e f_e)\mathrm{d}\Omega_{\mathbf{v}} + \frac{1}{2}\left(\varepsilon_0\mathbf{E}^2 + \frac{\mathbf{B}^2}{\mu_0}\right)\right]\mathrm{d}\Omega_{\mathbf{x}}. \tag{25}$$

The corresponding invariants for the Fourier-transformed Vlasov–Maxwell system are:

$$\|\hat{f}_\alpha\|^2 = \frac{1}{(2\pi)^3}\int_{\Omega_{\mathbf{x}}}\int_{\Omega_{\boldsymbol{\eta}}} |\hat{f}_\alpha|^2 \mathrm{d}\Omega_{\boldsymbol{\eta}}\mathrm{d}\Omega_{\mathbf{x}}, \tag{26}$$

$$N_\alpha = \int_{\Omega_{\mathbf{x}}} (2\pi)^3 (\hat{f}_\alpha)_{\boldsymbol{\eta}=0}\mathrm{d}\Omega_{\mathbf{x}}, \tag{27}$$

$$\mathbf{p} = \int_{\Omega_{\mathbf{x}}} [-\mathrm{i}(2\pi)^3 \nabla_{\boldsymbol{\eta}}(m_i f_i + m_e f_e)_{\boldsymbol{\eta}=0} + \varepsilon_0 \mathbf{E}\times\mathbf{B}]\mathrm{d}\Omega_{\mathbf{x}} \tag{28}$$

and

$$W = \int_{\Omega_{\mathbf{x}}} \left[-\frac{1}{2}(2\pi)^3 \nabla^2_{\boldsymbol{\eta}}(m_i f_i + m_e f_e)_{\boldsymbol{\eta}=0} + \frac{1}{2}\left(\varepsilon_0 \mathbf{E}^2 + \frac{\mathbf{B}^2}{\mu_0}\right)\right]\mathrm{d}\Omega_{\mathbf{x}}, \tag{29}$$

respectively, where the norm (26) follows from (22) via the Parseval relation. These invariants can be used to check the accuracy of the numerical scheme. When the system is restricted to a bounded domain in $\boldsymbol{\eta}$ space with appropriate boundary conditions (discussed in Section 2.4 below), the norm $\|\hat{f}_\alpha\|^2$ will be a non-increasing, positive function of time, while the other three quantities will still be conserved.

2.2. The normalized system of equations

In terms of primed, dimensionless variables

$$t = \omega_{\mathrm{pe}}^{-1} t', \quad \mathbf{v} = v_{\mathrm{Te}}\mathbf{v}', \quad \mathbf{x} = r_{\mathrm{De}}\mathbf{x}', \tag{30}$$

$$\boldsymbol{\eta} = v_{\mathrm{Te}}^{-1}\boldsymbol{\eta}', \quad \hat{f}_\alpha = n_0 \hat{f}'_\alpha, \quad f_\alpha = n_0 v_{\mathrm{Te}}^{-3} f'_\alpha, \tag{31}$$

$$\mathbf{E} = v_{\mathrm{Te}}^2 r_{\mathrm{De}}^{-1}(m_e/e)\mathbf{E}', \quad \Phi = v_{\mathrm{Te}}^2(m_e/e)\Phi', \quad \mathbf{B} = \omega_{\mathrm{pe}}(m_e/e)\mathbf{B}', \tag{32}$$

$$\mathbf{A} = v_{\mathrm{Te}}(m_e/e)\mathbf{A}', \quad \boldsymbol{\Gamma} = \omega_{\mathrm{pe}} v_{\mathrm{Te}}(m_e/e)\boldsymbol{\Gamma}', \quad \rho = e n_0 \rho', \tag{33}$$

$$\mathbf{j} = e n_0 v_{\mathrm{Te}} \mathbf{j}', \tag{34}$$

where $\omega_{\mathrm{pe}} = (n_0 e^2/\varepsilon_0 m_e)^{1/2}$ is the electron plasma frequency, n_0 is the background electron number density, $v_{\mathrm{Te}} = (k_B T_e/m_e)^{1/2}$ is the electron thermal speed, $r_{\mathrm{De}} = v_{\mathrm{Te}}/\omega_{\mathrm{pe}}$ is the electron Debye length, T_e is the electron temperature and k_B is the Boltzmann constant, the Fourier transformed Vlasov equation (18) can be cast into the normalized form (omitting the primes)

$$\frac{\partial \hat{f}_\alpha}{\partial t} - \mathrm{i}\nabla_{\mathbf{x}}\cdot\nabla_{\boldsymbol{\eta}}\hat{f}_\alpha - \frac{Q_\alpha}{M_\alpha}\left\{\mathrm{i}\mathbf{E}\cdot\boldsymbol{\eta}\hat{f}_\alpha + \nabla_{\boldsymbol{\eta}}\cdot\left[(\mathbf{B}\times\boldsymbol{\eta})\hat{f}_\alpha\right]\right\} = 0, \tag{35}$$

where $Q_\alpha = q_\alpha/e$ and $M_\alpha = m_\alpha/m_e$ (here $Q_i = 1$, $Q_e = -1$, $M_i = m_i/m_e$, and $M_e = 1$). The normalized equations for the potentials, (13) and (14), coupled with Eqs. (15) and (7), are

$$\frac{\partial \mathbf{A}}{\partial t} = \boldsymbol{\Gamma}, \qquad \frac{\partial \boldsymbol{\Gamma}}{\partial t} = \frac{c^2}{v_{\mathrm{Te}}^2}\nabla^2_{\mathbf{x}}\mathbf{A} + \mathbf{j}, \tag{36}$$

$$-\nabla^2_{\mathbf{x}}\Phi = \rho + \nabla_{\mathbf{x}}\cdot\boldsymbol{\Gamma} \tag{37}$$

and

$$\mathbf{E} = -\nabla_{\mathbf{x}}\Phi - \boldsymbol{\Gamma}, \tag{38}$$

$$\mathbf{B} = \mathbf{B}_0 + \nabla_{\mathbf{x}}\times\mathbf{A}, \tag{39}$$

respectively. Using Eqs. (20) and (21) in Eq. (4), the normalized charge and current densities are obtained as

$$\rho = (2\pi)^3[\Re(\hat{f}_i)_{\boldsymbol{\eta}=0} - \Re(\hat{f}_e)_{\boldsymbol{\eta}=0}] \tag{40}$$

and

$$\mathbf{j} = (2\pi)^3[\nabla_{\boldsymbol{\eta}}\Im(\hat{f}_i)_{\boldsymbol{\eta}=0} - \nabla_{\boldsymbol{\eta}}\Im(\hat{f}_e)_{\boldsymbol{\eta}=0}], \tag{41}$$

respectively.

2.3. Restriction to a bounded domain

In order to adapt the Fourier transformed Vlasov Maxwell system for numerical simulations, it must be restricted to a bounded domain. The computational domain is restricted to $0 \leqslant x_1 < L_1$, $0 \leqslant x_2 < L_2$, $0 \leqslant x_3 < L_3$, $0 \leqslant \eta_1 \leqslant \eta_{1\alpha,\max}$, $-\eta_{2\alpha,\max} \leqslant \eta_2 \leqslant \eta_{2\alpha,\max}$ and $-\eta_{3\alpha,\max} \leqslant \eta_3 \leqslant \eta_{3\alpha,\max}$. Here α (equal to e for electrons and i for ions) is introduced so that different domain sizes can be used in $\boldsymbol{\eta}$ space for the ion and electron distribution functions. For negative η_1, the symmetry (19) is used to obtain function values; it is therefore not necessary to numerically represent the solution for negative η_1 if the solution is represented for negative η_2 and η_3.

2.4. Well-posed boundary conditions

In this section, we will derive well-posed boundary conditions for the Vlasov equation in $\boldsymbol{\eta}$ space. Writing out the terms of the Fourier transformed Vlasov equation (35), we have

$$\frac{\partial \hat{f}_\alpha}{\partial t} - \mathrm{i}\frac{\partial^2 \hat{f}_\alpha}{\partial x_1 \partial \eta_1} - \mathrm{i}\frac{\partial^2 \hat{f}_\alpha}{\partial x_2 \partial \eta_2} - \mathrm{i}\frac{\partial^2 \hat{f}_\alpha}{\partial x_3 \partial \eta_3} - \frac{Q_\alpha}{M_\alpha}\left[\mathrm{i}(E_1\eta_1 + E_2\eta_2 + E_3\eta_3)\hat{f}_\alpha + (B_2\eta_3 - B_3\eta_2)\frac{\partial \hat{f}_\alpha}{\partial \eta_1} + (B_3\eta_1 - B_1\eta_3)\frac{\partial \hat{f}_\alpha}{\partial \eta_2} + (B_1\eta_2 - B_2\eta_1)\frac{\partial \hat{f}_\alpha}{\partial \eta_3}\right] = 0. \tag{42}$$

In configuration space, periodic boundary conditions

$$\hat{f}_\alpha(x_1 + L_1, x_2, x_3, \eta_1, \eta_2, \eta_3, t) = \hat{f}_\alpha(x_1, x_2, x_3, \eta_1, \eta_2, \eta_3, t), \tag{43}$$

$$\hat{f}_\alpha(x_1, x_2 + L_2, x_3, \eta_1, \eta_2, \eta_3, t) = \hat{f}_\alpha(x_1, x_2, x_3, \eta_1, \eta_2, \eta_3, t), \tag{44}$$

$$\hat{f}_\alpha(x_1, x_2, x_3 + L_3, \eta_1, \eta_2, \eta_3, t) = \hat{f}_\alpha(x_1, x_2, x_3, \eta_1, \eta_2, \eta_3, t), \tag{45}$$

are used for both the distribution functions and the electromagnetic fields. The artificial boundaries at $\eta_1 = \eta_{1\alpha,\max}$, $\eta_2 = \pm\eta_{2\alpha,\max}$ and $\eta_3 = \pm\eta_{3\alpha,\max}$ must be treated with care so that they do not give rise to reflections of waves or to instabilities. The strategy is to let outgoing waves pass over the boundaries, and to set incoming waves to zero. The problem of separating outgoing waves from incoming waves is solved by employing the spatial Fourier series expansions (transforms). In order to explore the idea, one can study the reduced initial value problem with a constant external magnetic field $\mathbf{B} = \mathbf{B}_0$ and a zero electric field $\mathbf{E} = 0$,

$$\frac{\partial \hat{f}_\alpha}{\partial t} - \mathrm{i}\frac{\partial^2 \hat{f}_\alpha}{\partial x_1 \partial \eta_1} - \mathrm{i}\frac{\partial^2 \hat{f}_\alpha}{\partial x_2 \partial \eta_2} - \mathrm{i}\frac{\partial^2 \hat{f}_\alpha}{\partial x_3 \partial \eta_3} - \frac{Q_\alpha}{M_\alpha}\left[(B_{2,0}\eta_3 - B_{3,0}\eta_2)\frac{\partial \hat{f}_\alpha}{\partial \eta_1} + (B_{3,0}\eta_1 - B_{1,0}\eta_3)\frac{\partial \hat{f}_\alpha}{\partial \eta_2} + (B_{1,0}\eta_2 - B_{2,0}\eta_1)\frac{\partial \hat{f}_\alpha}{\partial \eta_3}\right] = 0, \tag{46}$$

$$\hat{f}_\alpha(x_1, x_2, x_3, \eta_1, \eta_2, \eta_3, t)_{t=0} = \hat{f}_{\alpha 0}(x_1, x_2, x_3, \eta_1, \eta_2, \eta_3). \tag{47}$$

By introducing the spatial Fourier series pairs in (x_1, x_2, x_3) space,

$$\tilde{\phi}_{1,i_1} = \mathrm{F}_1\phi_1 = \frac{1}{L_1}\int_0^{L_1} \phi_1(x_1)\mathrm{e}^{-\mathrm{i}k_{x_1}x_1}\mathrm{d}x_1 \tag{48}$$

$$\phi_1 = \mathrm{F}_1^{-1}\tilde{\phi}_1 = \sum_{i_1=-\infty}^{\infty} \tilde{\phi}_{1,i_1}\mathrm{e}^{\mathrm{i}k_{x_1}x_1} \tag{49}$$

$$k_{x_1} = \frac{2\pi i_1}{L_1}, \quad i_1 = 0, \pm 1, \pm 2, \ldots, \tag{50}$$

$$\tilde{\phi}_{2,i_2} = \mathrm{F}_2\phi_2 = \frac{1}{L_2}\int_0^{L_2} \phi_2(x_2)\mathrm{e}^{-\mathrm{i}k_{x_2}x_2}\mathrm{d}x_2 \tag{51}$$

$$\phi_2 = \mathrm{F}_2^{-1}\tilde{\phi}_2 = \sum_{i_2=-\infty}^{\infty} \tilde{\phi}_{2,i_2} \mathrm{e}^{\mathrm{i}k_{x_2}x_2} \tag{52}$$

$$k_{x_2} = \frac{2\pi i_2}{L_2}, \quad i_2 = 0, \pm 1, \pm 2, \ldots \tag{53}$$

and

$$\tilde{\phi}_{3,i_3} = \mathrm{F}_3\phi_3 = \frac{1}{L_3}\int_0^{L_3} \phi_3(x_3)\mathrm{e}^{-\mathrm{i}k_{x_3}x_3}\mathrm{d}x_3, \tag{54}$$

$$\phi_3 = \mathrm{F}_3^{-1}\tilde{\phi}_3 = \sum_{i_3=-\infty}^{\infty} \tilde{\phi}_{3,i_3} \mathrm{e}^{\mathrm{i}k_{x_3}x_3}, \tag{55}$$

$$k_{x_3} = \frac{2\pi i_3}{L_3}, \quad i_3 = 0, \pm 1, \pm 2, \ldots \tag{56}$$

respectively, and Fourier-transforming Eq. (46) in all spatial directions, one obtains a new differential equation for the unknown function $\tilde{f}(k_{x_1}, k_{x_2}, k_{x_3}, \eta_1, \eta_2, \eta_3, t)$,

$$\frac{\partial \tilde{f}_\alpha}{\partial t} + \left[k_{x_1} - \frac{Q_\alpha}{M_\alpha}(B_{2,0}\eta_3 - B_{3,0}\eta_2)\right]\frac{\partial \tilde{f}_\alpha}{\partial \eta_1} + \left[k_{x_2} - \frac{Q_\alpha}{M_\alpha}(B_{3,0}\eta_1 - B_{1,0}\eta_3)\right]\frac{\partial \tilde{f}_\alpha}{\partial \eta_2} + \left[k_{x_3} - \frac{Q_\alpha}{M_\alpha}(B_{1,0}\eta_2 - B_{2,0}\eta_1)\right]\frac{\partial \tilde{f}_\alpha}{\partial \eta_3} = 0, \tag{57}$$

$$\tilde{f}_\alpha(k_{x_1}, k_{x_2}, k_{x_3}, \eta_1, \eta_2, \eta_3, t)_{t=0} = \tilde{f}_{\alpha 0}(k_{x_1}, k_{x_2}, k_{x_3}, \eta_1, \eta_2, \eta_3). \tag{58}$$

Eq. (57) is a hyperbolic equation for which the initial values are transported along the characteristic curves, given by

$$\frac{\mathrm{d}\eta_1(t)}{\mathrm{d}t} = k_{x_1} - \frac{Q_\alpha}{M_\alpha}(B_{2,0}\eta_3 - B_{3,0}\eta_2), \tag{59}$$

$$\frac{\mathrm{d}\eta_2(t)}{\mathrm{d}t} = k_{x_2} - \frac{Q_\alpha}{M_\alpha}(B_{3,0}\eta_1 - B_{1,0}\eta_3), \tag{60}$$

$$\frac{\mathrm{d}\eta_3(t)}{\mathrm{d}t} = k_{x_3} - \frac{Q_\alpha}{M_\alpha}(B_{1,0}\eta_2 - B_{2,0}\eta_1). \tag{61}$$

Along the boundary $\eta_1 = \eta_{\alpha 1,\max}$, Eq. (59) describes an *outflow* of data when $k_{x_1} - (Q_\alpha/M_\alpha)(B_{2,0}\eta_3 - B_{3,0}\eta_2) > 0$ and an *inflow* of data when $k_{x_1} - (Q_\alpha/M_\alpha)(B_{2,0}\eta_3 - B_{3,0}\eta_2) < 0$. A well-posed boundary condition is to set the inflow to zero at the boundary, i.e.,

$$(\tilde{f}_\alpha)_{\eta_1=\eta_{\alpha 1,\max}} = 0, \quad k_{x_1} - \frac{Q_\alpha}{M_\alpha}(B_{2,0}\eta_3 - B_{3,0}\eta_2) < 0, \tag{62}$$

which can be expressed with the help of the Heaviside step function H as

$$\tilde{f}_\alpha = H\left[k_{x_1} - \frac{Q_\alpha}{M_\alpha}(B_{2,0}\eta_3 - B_{3,0}\eta_2)\right]\tilde{f}_\alpha, \quad \eta_1 = \eta_{\alpha 1,\max}, \tag{63}$$

where

$$H(\xi) = \begin{cases} 1, & \xi \geqslant 0, \\ 0, & \xi < 0. \end{cases} \tag{64}$$

The boundary condition (63) allows outgoing waves to pass over the boundary and to be removed, while incoming waves are set to zero; the removal of the outgoing waves corresponds to the losing of information about the finest structures in velocity space. Inverse Fourier transforming Eq. (63) then gives the boundary condition for the original problem (46) as

$$\hat{f}_\alpha = \mathrm{F}_1^{-1} H\left[k_{x_1} - \frac{Q_\alpha}{M_\alpha}(B_{2,0}\eta_3 - B_{3,0}\eta_2)\right]\mathrm{F}_1\hat{f}_\alpha, \quad \eta_1 = \eta_{\alpha 1,\max}. \tag{65}$$

The operator $\mathrm{F}_1^{-1}H[k_{x_1} - (Q_\alpha/M_\alpha)(B_{2,0}\eta_3 - B_{3,0}\eta_2)]\mathrm{F}_1$ is a projection operator which removes incoming waves at the boundary $\eta_1 = \eta_{\alpha 1,\max}$. Similarly, the boundary conditions at $\eta_2 = \pm\eta_{\alpha 2,\max}$ and $\eta_3 = \pm\eta_{\alpha 3,\max}$ become

$$\hat{f}_\alpha = \mathrm{F}_2^{-1} H\left[k_{x_2} - \frac{Q_\alpha}{M_\alpha}(B_{3,0}\eta_1 - B_{1,0}\eta_3)\right]\mathrm{F}_2\hat{f}_\alpha, \quad \eta_2 = \eta_{\alpha 2,\max}, \tag{66}$$

$$\hat{f}_\alpha = \mathrm{F}_2^{-1} H\left[-k_{x_2} + \frac{Q_\alpha}{M_\alpha}(B_{3,0}\eta_1 - B_{1,0}\eta_3)\right]\mathrm{F}_2\hat{f}_\alpha, \quad \eta_2 = -\eta_{\alpha 2,\max}, \tag{67}$$

and

$$\hat{f}_\alpha = \mathrm{F}_3^{-1} H\left[k_{x_3} - \frac{Q_\alpha}{M_\alpha}(B_{1,0}\eta_2 - B_{2,0}\eta_1)\right]\mathrm{F}_3\hat{f}_\alpha, \quad \eta_3 = \eta_{\alpha 3,\max}, \tag{68}$$

$$\hat{f}_\alpha = \mathrm{F}_3^{-1} H\left[-k_{x_3} + \frac{Q_\alpha}{M_\alpha}(B_{1,0}\eta_2 - B_{2,0}\eta_1)\right]\mathrm{F}_3\hat{f}_\alpha, \quad \eta_3 = -\eta_{\alpha 3,\max}, \tag{69}$$

respectively.

In order to find well-posed boundary conditions in $\boldsymbol{\eta}$ space in the case when $\mathbf{B}$ varies both in space and time, Eq. (42) is rewritten in the form

$$\begin{aligned}\frac{\partial \hat{f}_\alpha}{\partial t} &+ \exp\left[\mathrm{i}\int_0^{x_1}(\beta_1 - \beta_{01})\mathrm{d}x_1\right]\frac{\partial}{\partial \eta_1}\left[-\mathrm{i}\frac{\partial}{\partial x_1} - \beta_{01}\right]G_{\alpha 1} + \exp\left[\mathrm{i}\int_0^{x_2}(\beta_2 - \beta_{02})\mathrm{d}x_2\right]\frac{\partial}{\partial \eta_2}\left[-\mathrm{i}\frac{\partial}{\partial x_2} - \beta_{02}\right]G_{\alpha 2} \\ &+ \exp\left[\mathrm{i}\int_0^{x_3}(\beta_3 - \beta_{03})\mathrm{d}x_3\right]\frac{\partial}{\partial \eta_3}\left[-\mathrm{i}\frac{\partial}{\partial x_3} - \beta_{03}\right]G_{\alpha 3} + \mathrm{i}(E_1\eta_1 + E_2\eta_2 + E_3\eta_3)\hat{f}_\alpha = 0,\end{aligned} \tag{70}$$

where the functions $G_{\alpha 1}$, $G_{\alpha 2}$ and $G_{\alpha 3}$ are defined as

$$G_{\alpha 1} = \hat{f}_\alpha \exp\left[-\mathrm{i}\int_0^{x_1}(\beta_1 - \beta_{01})\mathrm{d}x_1\right], \tag{71}$$

$$G_{\alpha 2} = \hat{f}_\alpha \exp\left[-\mathrm{i}\int_0^{x_2}(\beta_2 - \beta_{02})\mathrm{d}x_2\right], \tag{72}$$

and

$$G_{\alpha 3} = \hat{f}_\alpha \exp\left[-\mathrm{i}\int_0^{x_3}(\beta_3 - \beta_{03})\mathrm{d}x_3\right], \tag{73}$$

respectively, and where

$$\beta_1 = \frac{Q_\alpha}{M_\alpha}(B_2\eta_3 - B_3\eta_2), \quad \beta_{01} = \frac{1}{L_1}\int_0^{L_1}\beta_1\mathrm{d}x_1, \tag{74}$$

$$\beta_2 = \frac{Q_\alpha}{M_\alpha}(B_3\eta_1 - B_1\eta_3), \quad \beta_{02} = \frac{1}{L_2}\int_0^{L_2}\beta_2\mathrm{d}x_2 \tag{75}$$

and

$$\beta_3 = \frac{Q_\alpha}{M_\alpha}(B_1\eta_2 - B_2\eta_1), \quad \beta_{03} = \frac{1}{L_3}\int_0^{L_3}\beta_3\mathrm{d}x_3. \tag{76}$$

The form (70) of the Vlasov equation makes it possible to introduce stable numerical boundary conditions in $\boldsymbol{\eta}$ space in a systematic manner, as will be shown in Section 3.2. One also notes that $\int_0^{x_1}(\beta_1 - \beta_{01})\mathrm{d}x_1$, $\int_0^{x_2}(\beta_2 - \beta_{02})\mathrm{d}x_2$ and $\int_0^{x_3}(\beta_3 - \beta_{03})\mathrm{d}x_3$ are continuous and periodic in $\mathbf{x}$ space if $\mathbf{B}$ is continuous and periodic in $\mathbf{x}$; this is the reason for the subtraction of the mean values β_{01}, β_{02} and β_{03} in the integrals.

By studying the flow of data in the η_1, η_2 and η_3 directions for the auxiliary functions G_1, G_2 and G_3, respectively, one finds the outflow boundary conditions to be

$$G_{\alpha 1} = \mathrm{F}_1^{-1} H(k_{x_1} - \beta_{01}) \mathrm{F}_1 G_{\alpha 1}, \quad \eta_1 = \eta_{\alpha 1,\max}, \tag{77}$$

$$G_{\alpha 2} = \mathrm{F}_2^{-1} H(k_{x_2} - \beta_{02}) \mathrm{F}_2 G_{\alpha 2}, \quad \eta_2 = \eta_{\alpha 2,\max}, \tag{78}$$

$$G_{\alpha 2} = \mathrm{F}_2^{-1} H(-k_{x_2} + \beta_{02}) \mathrm{F}_2 G_{\alpha 2}, \quad \eta_2 = -\eta_{\alpha 2,\max}, \tag{79}$$

$$G_{\alpha 3} = \mathrm{F}_3^{-1} H(k_{x_3} - \beta_{03}) \mathrm{F}_3 G_{\alpha 3}, \quad \eta_2 = \eta_{\alpha 2,\max}, \tag{80}$$

$$G_{\alpha 3} = \mathrm{F}_3^{-1} H(-k_{x_3} + \beta_{03}) \mathrm{F}_3 G_{\alpha 3}, \quad \eta_2 = -\eta_{\alpha 2,\max}. \tag{81}$$

In the case when **B** is independent of **x** and t, the boundary conditions (77) and (78) reduce to the conditions (65)–(69). In the case where the domain is extended to negative η_1, there will be a boundary condition

$$G_{\alpha 1} = \mathrm{F}_1^{-1} H(-k_{x_1} + \beta_{01}) \mathrm{F}_1 G_{\alpha 1}, \quad \eta_1 = -\eta_{\alpha 1,\max}, \tag{82}$$

which will be used in the numerical scheme; see Section 3.2 below. Using the definitions (71)–(73) in Eqs. (77)–(82) and solving for $\hat{f}_\alpha$ yields the boundary conditions for $\hat{f}_\alpha$.

A proof of the well-posedness of the continuous problem with the given boundary conditions is given in the Appendix.

3. The numerical approach

3.1. Discretization

The computational domain is discretized on a rectangular, equidistant grid, where the particle distribution functions of species α are discretized and enumerated such that $\hat{f}_\alpha(x_{1,i_1}, x_{2,i_2}, x_{3,i_3}, \eta_{1,\alpha,j_1}, \eta_{2,\alpha,j_2}, \eta_{3,\alpha,j_3}, t_k) \approx \hat{f}^k_{\alpha,i_1,i_2,i_3,j_1,j_2,j_3}$. The scalar potential is discretized as $\Phi(x_{1,i_1}, x_{2,i_2}, x_{3,i_3}, t_k) \approx \Phi^k_{i_1,i_2,i_3}$, and the vector components E_1, E_2, E_3, B_1, B_2, B_3, A_1, A_2, A_3, Γ_1, Γ_2 and Γ_3 are discretized in the same manner. The spatial variables are discretized as $x_{1,i_1} = i_1 \Delta x_1$, $i_1 = 0, 1, \ldots, N_{x_1} - 1$, $x_{2,i_2} = i_2 \Delta x_2$, $i_2 = 0, 1, \ldots, N_{x_2} - 1$ and $x_{3,i_3} = i_3 \Delta x_3$, $i_3 = 0, 1, \ldots, N_{x_3} - 1$, the Fourier transformed velocity variables are discretized as $\eta_{1,\alpha,j_1} = j_1 \Delta \eta_{1,\alpha}$, $j_1 = 0, 1, \ldots, N_{\eta_1}$, $\eta_{2,\alpha,j_2} = j_2 \Delta \eta_{2,\alpha}$, $j_2 = -N_{\eta_2}, \ldots, -1, 0, 1, \ldots, N_{\eta_2}$, and $\eta_{3,\alpha,j_3} = j_3 \Delta \eta_{3,\alpha}$, $j_3 = -N_{\eta_3} \ldots -1, 0, 1, \ldots, N_{\eta_3}$. The grid sizes are $\Delta x_1 = L_1/N_{x_1}$, $\Delta x_2 = L_2/N_{x_2}$, $\Delta x_3 = L_3/N_{x_3}$, $\Delta \eta_{1,\alpha} = \eta_{\alpha 1,\max}/N_{\eta_1}$, $\Delta \eta_{2,\alpha} = \eta_{\alpha 2,\max}/N_{\eta_2}$ and $\Delta \eta_{3,\alpha} = \eta_{\alpha 3,\max}/N_{\eta_3}$. For convenience, only even numbers will be used for N_{x_1}, N_{x_2} and N_{x_3} when they are larger than unity. The time is discretized as $t_k = t_{k-1} + \Delta t_k$, $t_0 = 0$, $k = 1, 2, \ldots, N_t$. The time step Δt_k can either be fixed or calculated adaptively; see the stability conditions discussed in Section 3.3.

3.2. Numerical approximations

The Vlasov equation (70) for the ions and electrons, and the wave equation (36) are discretized in **x** and $\boldsymbol{\eta}$ space. The discretized solution $\hat{f}_i$, $\hat{f}_e$, **A** and $\boldsymbol{\Gamma}$ can formally be ordered into a solution vector **Y**. We denote by **P**(**Y**) the discretized right-hand sides of the Vlasov equations and the wave equation when the time-derivatives only are moved to the left-hand sides. This yields the semi-discretization

$$\frac{\mathrm{d}\mathbf{Y}}{\mathrm{d}t} = \mathbf{P}(\mathbf{Y}). \tag{83}$$

The grid function **P** involves e.g. the terms differentiated numerically by **x** and $\boldsymbol{\eta}$ in the Vlasov and wave equations, where the electromagnetic fields **E** and **B** are *functions* of **Y** via the definitions (38) and (39) and the implicit Eq. (37) for the potential. With this definition, time steps are taken with the fourth-order Runge–Kutta method,

(1) $\mathbf{K}^{(1)} \leftarrow \mathbf{P}(\mathbf{Y}^k)$,

(2) $\mathbf{K}^{(2)} \leftarrow \mathbf{P}(\mathbf{Y}^k + \mathbf{K}^{(1)} \Delta t/2)$,

(3) $\mathbf{K}^{(3)} \leftarrow \mathbf{P}(\mathbf{Y}^k + \mathbf{K}^{(2)} \Delta t/2)$,

(4) $\mathbf{K}^{(4)} \leftarrow \mathbf{P}(\mathbf{Y}^k + \mathbf{K}^{(3)} \Delta t)$,

(5) $\mathbf{Y}^{k+1} \leftarrow \mathbf{Y}^k + \dfrac{\Delta t}{6}(\mathbf{K}^{(1)} + 2\mathbf{K}^{(2)} + 2\mathbf{K}^{(3)} + \mathbf{K}^{(4)})$.

We now turn to the approximations of $\mathbf{x}$ and $\boldsymbol{\eta}$ derivatives needed to calculate the right-hand side $\mathbf{P}(\mathbf{Y})$. The steps needed for obtaining the approximation $\mathbf{P}$ are:

(1) Calculate the electric and magnetic fields field numerically from Eqs. (37)–(39), using the present Runge–Kutta stage of $\hat{f}_i$, $\hat{f}_e$, $\mathbf{A}$ and $\boldsymbol{\Gamma}$.
(2) Calculate a numerical approximation of the terms involving $\mathbf{x}$ and $\boldsymbol{\eta}$ derivatives in the Vlasov equation (70), for all points, including the points along the boundaries $\eta_1 = \eta_{\alpha 1,\max}$, $\eta_2 = \pm\eta_{\alpha 2,\max}$ and $\eta_3 = \pm\eta_{\alpha 3,\max}$.

In $\mathbf{x}$ space a pseudo-spectral method (trigonometric interpolations) is employed to calculate the $\mathbf{x}$ derivatives and the integration of Eq. (37) accurately. The Fourier transform and its inverse is approximated by the discrete Fourier transform and inverse discrete Fourier transform, respectively, via the fast Fourier transform (FFT) and inverse fast Fourier transform (IFFT) algorithms. For the Fourier transformation in x_1, x_2 and x_3 space, the symbolic notations $\mathrm{F}_1 \approx \mathrm{FFT}_1$, $\mathrm{F}_2 \approx \mathrm{FFT}_2$ and $\mathrm{F}_3 \approx \mathrm{FFT}_3$, respectively, will be used, while for the inverse Fourier transforms we use $\mathrm{F}_1^{-1} \approx \mathrm{IFFT}_1$, $\mathrm{F}_2^{-1} \approx \mathrm{IFFT}_2$ and $\mathrm{F}_3^{-1} \approx \mathrm{IFFT}_3$, respectively.

The approximations of the x_1, x_2 and x_3 derivatives are obtained as

$$\frac{\partial \psi}{\partial x_1} \approx \mathrm{IFFT}_1[\mathrm{i}k_{x_1}\mathrm{FFT}_1(\psi)], \tag{84}$$

$$\frac{\partial \psi}{\partial x_2} \approx \mathrm{IFFT}_2[\mathrm{i}k_{x_2}\mathrm{FFT}_2(\psi)] \tag{85}$$

and

$$\frac{\partial \psi}{\partial x_3} \approx \mathrm{IFFT}_3\left[\mathrm{i}k_{x_3}\mathrm{FFT}_3(\psi)\right], \tag{86}$$

respectively, where the components of the wave-numbers are $(k_{x_1})_{i_1} = 2\pi i_1/L_1$ with $i_1 = -(N_{x_1}/2-1),\ldots,(N_{x_1}/2)$, $(k_{x_2})_{i_2} = 2\pi i_2/L_2$ with $i_2 = -(N_{x_2}/2-1),\ldots,(N_{x_2}/2)$ and $(k_{x_3})_{i_3} = 2\pi i_3/L_3$ with $i_3 = -(N_{x_3}/2-1),\ldots,(N_{x_3}/2)$. A problem is that the highest Fourier components, corresponding to $i_1 = N_{x_1}/2$, $i_2 = N_{x_2}/2$ and $i_3 = N_{x_3}/2$, obtained in the FFT_1, FFT_2 and FFT_3 algorithms, are not well defined since they correspond exactly to the Nyqvist frequency, and in our numerical experiments they have given rise to numerical instabilities. Therefore these components are set to zero in the approximations of x_1, x_2 and x_3 derivatives in Eq. (70).

The scalar potential is integrated numerically from Eq. (37) as

$$\phi \approx \mathrm{IFFT}_3\mathrm{IFFT}_2\mathrm{IFFT}_1\left[\left(\frac{1}{k_{x_1}^2+k_{x_2}^2+k_{x_3}^2}\right)\mathrm{FFT}_3\mathrm{FFT}_2\mathrm{FFT}_1(\rho+\nabla_{\mathbf{x}}\cdot\boldsymbol{\Gamma})\right], \tag{87}$$

where the charge density is [cf. Eq. (40)] $\rho_{i1,i2,i3} = (2\pi)^3(\Re\hat{f}_{\mathrm{i},i1,i2,i3,0,0,0} - \Re\hat{f}_{\mathrm{e},i1,i2,i3,0,0,0})$, and the derivatives in the $\nabla_{\mathbf{x}}\cdot\boldsymbol{\Gamma}$ term is calculated using the approximations (84)–(86). The Fourier component corresponding to $k_{x_1} = k_{x_2} = k_{x_3} = 0$ is set to zero in Eq. (87).

In the expression (41) for the electric current, the gradient $\nabla_{\boldsymbol{\eta}}$ is approximated with sixth-order different schemes. We have for the η_1 derivative

$$\frac{\partial \Im(f_\alpha)_{\boldsymbol{\eta}=0}}{\partial \eta_1} \approx \frac{g_3^{(1)} - 9g_2^{(1)} + 45g_1^{(1)} - 45g_{-1}^{(1)} + 9g_{-2}^{(1)} - g_{-3}^{(1)}}{60\Delta\eta_{1,\alpha}} = \frac{g_3^{(1)} - 9g_2^{(1)} + 45g_1^{(1)}}{30\Delta\eta_{1,\alpha}}, \tag{88}$$

where the symbol $g_{j_1}^{(1)}$ is used for $\Im(\hat{f}_{\alpha,i_1,i_2,i_3,j_1,0,0})$ (omitting all indices but j_1). The last equality follows from the symmetry property (19). Similarly, we have for the η_2 and η_3 derivatives, respectively,

$$\frac{\partial \Im(f_\alpha)_{\boldsymbol{\eta}=0}}{\partial \eta_2} \approx= \frac{g_3^{(2)} - 9g_2^{(2)} + 45g_1^{(2)}}{30\Delta\eta_{2,\alpha}}, \tag{89}$$

where $g_{j_2}^{(2)}$ is used for $\Im(\hat{f}_{\alpha,i_1,i_2,i_3,0,j_2,0})$, and

$$\frac{\partial \Im(f_\alpha)_{\boldsymbol{\eta}=0}}{\partial \eta_3} \approx= \frac{g_3^{(3)} - 9g_2^{(3)} + 45g_1^{(3)}}{30\Delta\eta_{3,\alpha}}, \tag{90}$$

where $g_{j_3}^{(3)}$ is used for $\Im(\hat{f}_{\alpha,i_1,i_2,i_3,0,0,j_3})$.

The integrals used in Eqs. (70)–(73) are approximated, up to "constants" of integration which will have no effect on the numerical results, by

$$\int_0^{x_1} (\beta_1 - \beta_{01})\mathrm{d}x_1 \approx \mathrm{IFFT}_1 \frac{1}{\mathrm{i}k_{x_1}} \mathrm{FFT}_1(\beta_1 - \beta_{01}), \tag{91}$$

$$\int_0^{x_2} (\beta_2 - \beta_{02})\mathrm{d}x_2 \approx \mathrm{IFFT}_2 \frac{1}{\mathrm{i}k_{x_2}} \mathrm{FFT}_2(\beta_2 - \beta_{02}) \tag{92}$$

and

$$\int_0^{x_3} (\beta_3 - \beta_{03})\mathrm{d}x_3 \approx \mathrm{IFFT}_3 \frac{1}{\mathrm{i}k_{x_3}} \mathrm{FFT}_2(\beta_3 - \beta_{03}), \tag{93}$$

where the components corresponding to $k_{x_1} = 0$, $k_{x_2} = 0$ and $k_{x_3} = 0$ are set to zero in Eqs. (91)–(93), respectively.

The numerical approximation of the x_1 and η_1 derivatives in Eq. (70) are performed as

$$-\mathrm{i}\frac{\partial}{\partial \eta_1}\left(\frac{\partial}{\partial x_1} - \mathrm{i}\beta_{01}\right) G_{\alpha 1} \approx -\mathrm{iIFFT}_1\left\{\mathrm{D}_{\eta_1}[\mathrm{i}(k_{x_1} - \beta_{01})\mathrm{FFT}_1 G_{\alpha 1}]\right\}, \tag{94}$$

where D_{η_1} is a difference approximation of the η_1 derivative. The form of the approximation (94) makes it possible to separate between incoming and outgoing waves at the boundary and to use numerically stable approximations of the η_1 derivative for the two cases: The factor $(k_{x_1} - \beta_{01})$ appearing in Eq. (94) is the same factor as in the boundary condition (77); thus $(k_{x_1} - \beta_{01}) \geqslant 0$ describes outflow and $(k_{x_1} - \beta_{01}) < 0$ describes inflow at the boundary at $\eta_1 = \eta_{\alpha 1,\max}$.

For the numerical scheme used to calculate the η_1 derivative, we need function values for negative η_1. These function values are obtained by employing a symmetry relation similar to (19). In order to calculate the difference approximation D_{η_1} of the η_1 derivative used in Eq. (94), the symmetry is used to temporarily represent function values for negative η_1, as follows:

Before performing the η_1 differentiation, the function values are temporarily moved, by symmetry, from the part of the domain with positive η_1 and negative η_2 to the part of the domain with negative η_1 and positive η_2, so that the η_1 domain goes from $\eta_1 = -\eta_{\alpha 1,\max}$ to $\eta_1 = \eta_{\alpha 1,\max}$ and the η_2 domain goes from $\eta_2 = 0$ to $\eta_2 = \eta_{\alpha 2,\max}$. Thereafter the numerical η_1 differentiation is performed with appropriate boundary conditions, and finally the result is re-distributed to the original domain with only non-negative η_1.

In detail, these steps are performed as follows: The grid function to be differentiated numerically in Eq. (94) is

$$[\mathrm{i}(k_{x_1} - \beta_{01})\mathrm{FFT}_1 G_{\alpha 1}] \equiv \tilde{g}_{i_1,i_2,i_3,j_1,j_2,j_3}, \tag{95}$$

where $i_1 = -(N_{x_1}/2 - 1), \ldots, N_{x_1}/2$ now represents Fourier components $(k_{x_1})_{i_1} = i_1 2\pi/L_1$ of $\tilde{g}$ since the Fourier transform FFT_1 has been applied in the x_1 direction. Because of the Fourier transforms both in x_1 and $\mathbf{v}$ space (yielding k_{x_1}, η_1, η_2 and η_3), the grid function $\tilde{g}$ obeys the symmetry property, similar to Eq. (19),

$$\tilde{g}_{i_1,i_2,i_3,-j_1,j_2,j_3} = \tilde{g}^*_{-i_1,i_2,i_3,j_1,-j_2,-j_3} \tag{96}$$

i.e., in order to obtain the components of $\tilde{g}$ for negative j_1 (representing negative η_1), which are not represented on the numerical grid, the complex conjugates (superscript *) of these components are found

on the numerical grid by the symmetry relation at the location where i_1, j_1, j_2 and j_3 has opposite signs; therefore, in order to perform the η_1 derivative numerically, the components of $\tilde{g}$ are ordered in vectors as

$$\mathbf{g}_{i_1,i_2,i_3,j_2,j_3} = \begin{bmatrix} g_{-N_{\eta_1}} \\ g_{-N_{\eta_1}+1} \\ \vdots \\ g_{-1} \\ g_0 \\ g_1 \\ \vdots \\ g_{N_{\eta_1}} \end{bmatrix}_{i_1,i_2,i_3,j_2,j_3} \leftarrow \begin{bmatrix} \tilde{g}^*_{-i_1,i_2,i_3,N_{\eta_1},-j_2,-j_3} \\ \tilde{g}^*_{-i_1,i_2,i_3,N_{\eta_1}-1,-j_2,-j_3} \\ \vdots \\ \tilde{g}^*_{-i_1,i_2,i_3,1,-j_2,-j_3} \\ \tilde{g}_{i_1,i_2,i_3,0,j_2,j_3} \\ \tilde{g}_{i_1,i_2,i_3,1,j_2,j_3} \\ \vdots \\ \tilde{g}_{i_1,i_2,i_3,N_{\eta_1},j_2,j_3} \end{bmatrix} \tag{97}$$

for each $j_2 = 0, 1, \ldots, N_{\eta_2}$, $j_3 = -N_{\eta_3}, 1, \ldots, N_{\eta_3}$, $i_1 = -(N_{x_1}/2 - 1), \ldots, N_{x_1}/2$, $i_2 = 0, 1, \ldots, N_{x_2} - 1$ and $i_3 = 0, 1, \ldots, N_{x_3} - 1$.

The η_1 derivative $g' = \frac{\partial g}{\partial \eta_1} \approx \mathrm{D}_{\eta_1} \mathbf{g}_{i_1,i_2,i_3,j_2,j_3}$ is calculated using the standard fourth order Padé scheme [20,21]. For the inner points, the implicit approximation

$$g'_{j_1-1} + 4g'_{j_1} + g'_{j_1+1} = \frac{3}{\Delta\eta_1}(g_{j_1+1} - g_{j_1-1}), \tag{98}$$

where $j_1 = -N_{\eta_1} + 1, \ldots, -1, 0, 1, \ldots, N_{\eta_1} - 1$ is used.

The boundary at $\eta_1 = \eta_{\alpha 1,\max}$ is an *outflow* boundary for $k_{x_1} \geqslant \beta_{01}$ [cf. Eq. (77)], where $k_{x_1} = 2\pi i_1/L_1$, i.e., for $i_1 \geqslant L_1\beta_{01}/2\pi$. At the outflow boundary a one-sided approximation,

$$g'_{N_{\eta_1}} + 2g'_{N_{\eta_1}-1} = -\frac{1}{2\Delta\eta_1}(-5g_{N_{\eta_1}} + 4g_{N_{\eta_1}-1} + g_{N_{\eta_1}-2}) \tag{99}$$

is used, which gives a truncation error of order $\Delta\eta_1^3$ at the boundary. For $k_{x_1} < \beta_{01}$, the boundary at $\eta_1 = \eta_{\alpha 1,\max}$ is an *inflow* boundary, at which a straight extrapolation

$$g'_{N_{\eta_1}} = g'_{N_{\eta_1}-1} \tag{100}$$

is used, which gives a truncation error of order $\Delta\eta_1^2$ at the boundary.

Correspondingly, the schemes at $\eta_1 = -\eta_{\alpha 1,\max}$ becomes

$$g'_{-N_{\eta_1}} + 2g'_{-N_{\eta_1}+1} = \frac{1}{2\Delta\eta_1}(-5g_{-N_{\eta_1}} + 4g_{-N_{\eta_1}+1} + g_{-N_{\eta_1}+2}) \tag{101}$$

and

$$g'_{-N_{\eta_1}} = g'_{-N_{\eta_1}+1} \tag{102}$$

for the *outflow* (where $k_{x_1} \leqslant \beta_{01}$) and *inflow* (where $k_{x_1} > \beta_{01}$) boundaries, respectively [cf. Eq. (80)].

The reason for using different approximations at the inflow and outflow boundaries is that the third-order approximation of the η_1 derivative used for the outflow of waves is not completely stable for the inflow of waves; numerical test has shown that there are some slowly growing modes which eventually destroy the numerical solution [18].

Eqs. (98)–(102) form a tridiagonal equation system for each component i_1, i_2, i_3, j_2 and j_3 in Eq. (97), each system having $2N_{\eta_1} + 1$ complex-valued unknowns. When the solution vector $\mathbf{g}'$ has been calculated, the numerical differentiation of $\tilde{g}$ is obtained as

$$\begin{bmatrix} \tilde{g}'_{-i_1,i_2,i_3,N_{\eta_1},-j_2,-j_3} \\ \tilde{g}'_{-i_1,i_2,i_3,N_{\eta_1}-1,-j_2,-j_3} \\ \vdots \\ \tilde{g}'_{-i_1,i_2,i_3,1,-j_2,-j_3} \\ \tilde{g}'_{i_1,i_2,i_3,0,j_2,j_3} \\ \tilde{g}'_{i_1,i_2,i_3,1,j_2,j_3} \\ \vdots \\ \tilde{g}'_{i_1,i_2,i_3,N_{\eta_1},j_2,j_3} \end{bmatrix} \leftarrow \begin{bmatrix} -(g')^*_{-N_{\eta_1}} \\ -(g')^*_{-N_{\eta_1}+1} \\ \vdots \\ -(g')^*_{-1} \\ g'_0 \\ g'_1 \\ \vdots \\ g'_{N_{\eta_1}} \end{bmatrix}_{i_1,i_2,i_3,j_2,j_3}, \tag{103}$$

i.e., it is used that for the η_1 derivative of $\tilde{g}$, the real part is an odd function with respect to (i_1, j_1, j_2, j_3) and the imaginary part is an even function with respect to the same indices; see a similar discussion after Eq. (19). Finally, the numerical inverse Fourier transform in x_1 space yields the approximation (94).

The algorithm above for calculating the x_1 and η_1 derivatives will, with small modifications, hold also for the differentiation in x_2 and η_2 space as well as in x_3 and η_3 space. The difference is that function values are already represented on the numerical grid for negative η_2 and η_3, and it is therefore not necessary to artificially extend function values to negative η_2 and η_3 by symmetry. For example, using approximations analogous to Eq. (94) in x_2 and η_2 space instead of x_1 and η_1 space, the η_2 differentiation is performed directly on the function

$$[\mathrm{i}(k_{x_2} - \beta_{02})\mathrm{FFT}_2 G_{\alpha 2}] \equiv \tilde{g}_{i_1,i_2,i_3,j_1,j_2,j_3} \tag{104}$$

with $j_1 = 0, 1, \ldots, N_{\eta_1}$, $j_2 = -N_{\eta_2}, 1, \ldots, N_{\eta_2}$, $i_1 = 0, \ldots, N_{x_1}$ and $i_2 = -(N_{x_2}/2 - 1), 1, \ldots, N_{x_2} - 1$, and taking into account the boundary condition (78). A similar discussion holds for the differentiation in x_3 and η_3 space.

Between each Runge–Kutta time-step, the boundary operators (77)–(81) are applied along the boundaries in $\boldsymbol{\eta}$ space in order to remove any spurious waves along these boundaries. The boundary operators are calculated by using the approximations (91)–(93) for the integrals, and the FFT algorithm is used to approximate the Fourier transforms.

In order to reduce aliasing effects in the $\mathbf{x}$ space for nonlinear problems, a sixth-order dissipative term

$$\delta \Delta x_1^4 \left(\frac{\partial^6 \hat{f}_\alpha}{\partial x_1^6} + \frac{\partial^6 \hat{f}}{\partial x_2^6} + \frac{\partial^6 \hat{f}}{\partial x_3^6} \right) \tag{105}$$

is added to the right-hand side of Eq. (70), where the constant δ is set to some small positive number. The derivatives are approximated by centered second-order approximations.

3.3. Stability constraints on the time step

The fourth-order Runge–Kutta time stepping scheme has the Courant condition [22]

$$\Delta t < \frac{\sqrt{8}}{\lambda_{\max}}, \tag{106}$$

which must be fulfilled for stability. Here $\lambda_{\max}$ is the maximum modulus of the eigenvalues of the semi-discretized Vlasov–Maxwell system. Carrying out a standard von Neumann analysis on the Vlasov equation (42), where the electric and magnetic fields are assumed to be locally constant in space and time, we have

$$\begin{aligned} \lambda_{\alpha,\max} =& K_{x_1} K_{\eta_1,\alpha} + K_{x_2} K_{\eta_2,\alpha} + K_{x_3} K_{\eta_3,\alpha} + |Q_\alpha/M_\alpha| [E_{1,\max}\eta_{1,\alpha,\max} + E_{2,\max}\eta_{2,\alpha,\max} + E_{3,\max}\eta_{3,\alpha,\max} \\ &+ (B_{2,\max}\eta_{\alpha 3,\max} + B_{3,\max}\eta_{\alpha 2,\max}) K_{\eta_1,\alpha} + (B_{3,\max}\eta_{\alpha 1,\max} + B_{1,\max}\eta_{\alpha 3,\max}) K_{\eta_2,\alpha} \\ &+ (B_{1,\max}\eta_{\alpha 2,\max} + B_{2,\max}\eta_{\alpha 1,\max}) K_{\eta_3,\alpha}], \end{aligned} \tag{107}$$

where $K_{x_1}, K_{x_2}, K_{x_3}, K_{\eta_1,\alpha}, K_{\eta_2,\alpha}$ and $K_{\eta_3,\alpha}$ are the maximum values of the approximations of wave-numbers produced by the numerical approximations of the derivatives in $\mathbf{x}$ and $\boldsymbol{\eta}$ space. They are given by

$$K_{x_1} = \frac{\pi}{\Delta x_1}, \quad K_{x_2} = \frac{\pi}{\Delta x_2}, \quad K_{x_3} = \frac{\pi}{\Delta x_3}, \tag{108}$$

$$K_{\eta_1,\alpha} = \frac{\sqrt{3}}{\Delta \eta_{1,\alpha}}, \quad K_{\eta_2,\alpha} = \frac{\sqrt{3}}{\Delta \eta_{2,\alpha}}, \quad K_{\eta_3,\alpha} = \frac{\sqrt{3}}{\Delta \eta_{3,\alpha}}, \tag{109}$$

where K_{x_1}, K_{x_2} and K_{x_3} are produced by the pseudo-spectral method and $K_{\eta_1,\alpha}, K_{\eta_2,\alpha}$ and $K_{\eta_3,\alpha}$ are produced by the Padé scheme. For the Maxwell equation, we have maximum eigenvalue

$$\lambda_{\mathrm{M,\,max}} = \frac{c}{v_{\mathrm{Te}}}\sqrt{K_{x1}^2 + K_{x2}^2 + K_{x3}^2}. \tag{110}$$

The the largest $\lambda_{\max}$ must be used in the stability condition, and we thus choose the time step as

$$\Delta t = \alpha \frac{\sqrt{8}}{\max(\lambda_{\mathrm{i,max}}, \lambda_{\mathrm{e,max}}, \lambda_{\mathrm{M,max}})}, \tag{111}$$

where the positive constant $\alpha < 1$ for stability. In the numerical experiments in the present article, we have used $\alpha = 0.9$. As $\lambda_{\max}$ varies with time, the time step Δt is adapted to maintain numerical stability.

The numerical stability of the artificial boundaries at $\eta_1 = \eta_{\alpha 1,\max}$, $\eta_2 = \pm\eta_{\alpha 2,\max}$ and $\eta_3 = \pm\eta_{\alpha 3,\max}$ has not been considered here, but we rely on the analysis of model problems performed by Lele [21] and by Gustafsson and Olsson [20] for the outflow boundaries, and on long-time numerical stability tests presented in Section 4 below.

3.4. The choice of domain and grid sizes

When using the numerical algorithm to solve physical problems, it is important to know what is the computational domain and resolution in the real velocity space, i.e., what are the maximum velocity components $v_{\alpha 1,\max}$, $v_{\alpha 2,\max}$, $v_{\alpha 3,\max}$, used in the real velocity space to resolve the particle distribution function of species α, and what are the grid sizes $\Delta v_{1,\alpha}$, $\Delta v_{2,\alpha}$ and $\Delta v_{3,\alpha}$ used in the numerical solution. For given $\eta_{j,\alpha,\max}$ and $\Delta\eta_{\alpha j}$, $j = 1, 2, 3$, the maximum represented velocity and the grid size in velocity space are given by

$$v_{\alpha j,\max} = \frac{\pi}{\Delta \eta_{j,\alpha}}, \tag{112}$$

and

$$\Delta v_{j,\alpha} = \frac{\pi}{\eta_{\alpha j,\max}}, \tag{113}$$

respectively. As a good rule of thumb, one should choose $\eta_{\alpha j,\max}$ and $\Delta\eta_{j,\alpha}$ such that the maximum velocity component is more than twice the maximum particle velocity one wants to resolve in the numerical solution, in order to avoid dispersive errors on the particle velocities [23].

4. Numerical results

4.1. Stability tests

In order to assess the numerical stability of the numerical scheme, including the boundary conditions in $\boldsymbol{\eta}$ space, we have performed long-time numerical tests where the electron and ion distribution initially functions are set to low-amplitude random numbers and the time evolution of the energy norms of the electron and ion distribution functions are followed. In the numerical simulations, we could not see any growing modes. Two examples are depicted in Fig. 1, where we have used a constant external magnetic field of amplitude 0.25 along the x_1 direction. In the simulations, we used the number of grid points $N_{x_1} = N_{x_2} = N_{x_3} = 10$ and $N_{\eta_1} = 2N_{\eta_2} = 2N_{\eta_3} = 16$, the domain sizes $L_1 = 2\pi \times 500$, $L_2 = L_3 = 2\pi \times 10^3$, $\eta_{\mathrm{e1,max}} = \eta_{\mathrm{e2,max}} = \eta_{\mathrm{e3,max}} = 6$

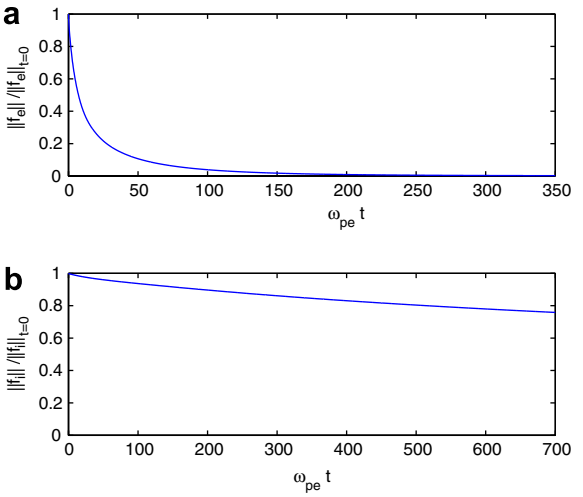

Fig. 1. The energy norm for (a) the electron and (b) the ion distribution function, normalized by their initial values. The distribution functions were initially set to random numbers of order 10^{-5}, and the solution was advanced in time with 3000 time steps in panel (a) and 6000 time steps in panel (b). The amplitude of the external magnetic field was set to $B_{01} = 0.25$ (in normalized units) and was directed along the x_1 axis.

and $\eta_{i1,\max} = \eta_{i2,\max} = \eta_{i3,\max} = 200$, and the constant time-step $\Delta t = 0.14$. We used the mass ratio $m_i/m_e = 400$. The energy norms in Fig. 1, which are approximated numerically as sum representations of the integral (26), are decreasing monotonically in agreement with the property of the energy norm shown in the Appendix. The energy norm for the ions is decreasing slower due to the less mobile ions. A case where the magnetic field varies in both space and time is shown in Fig. 6 below.

4.2. Electromagnetic electron waves

The general dispersion relation for electron waves in a cold collisionless plasma with an external magnetic field is given by the Appleton-Hartree dispersion relation [24]

$$\frac{c^2k^2}{\omega^2} = 1 - \frac{2\omega_{pe}^2(\omega^2 - \omega_{pe}^2)/\omega^2}{2(\omega^2 - \omega_{pe}^2) - \omega_{ce}^2\sin^2\theta \pm \omega_{ce}\Delta}, \tag{114}$$

where $\Delta = [\omega_{ce}^2\sin^4\theta + 4\omega^{-2}(\omega^2 - \omega_{pe}^2)^2\cos^2\theta]^{1/2}$ and θ is the angle between the external magnetic field and the wave vector. In order to assess that the Vlasov code reproduces these well-known wave modes in the plasma, we have simulated electromagnetic waves propagating at different angles to the magnetic field; see Figs. 2 and 3. In the simulations, we restricted the problem to one spatial dimension, along the x_1 axis, and used three velocity dimensions. The initial condition for the electron distribution function was a Maxwellian distribution (in normalized units)

$$\hat{f}_e = (2\pi)^{-3}\exp\left[-\frac{(\eta_1^2 + \eta_2^2 + \eta_3^2)}{2}\right], \tag{115}$$

while for the ions we used

$$\hat{f}_i = (2\pi)^{-3}\exp\left[-\frac{(\eta_1^2 + \eta_2^2 + \eta_3^2)}{2}\left(\frac{T_i m_e}{T_e m_i}\right)^{1/2}\right], \tag{116}$$

with $T_i/T_e = 100$ and $m_i/m_e = 1836$, and we chose $c/v_{Te} = 50$ for the electromagnetic waves. The magnetic field strength was chosen such that $\omega_{ce}/\omega_{pe} = 1/4$, i.e. in our scaled unit we have $|\mathbf{B}_0| = 1/4$. A low-amplitude noise (random numbers) were added to the vector potential $\mathbf{A}$ and to $\mathbf{\Gamma}$ so that all wave modes in the system were excited. The numerical parameters were chosen as $N_{x_1} = 40$, $N_{x_2} = N_{x_3} = 1$, $L_1 = \pi \times 10^3$ (corresponding

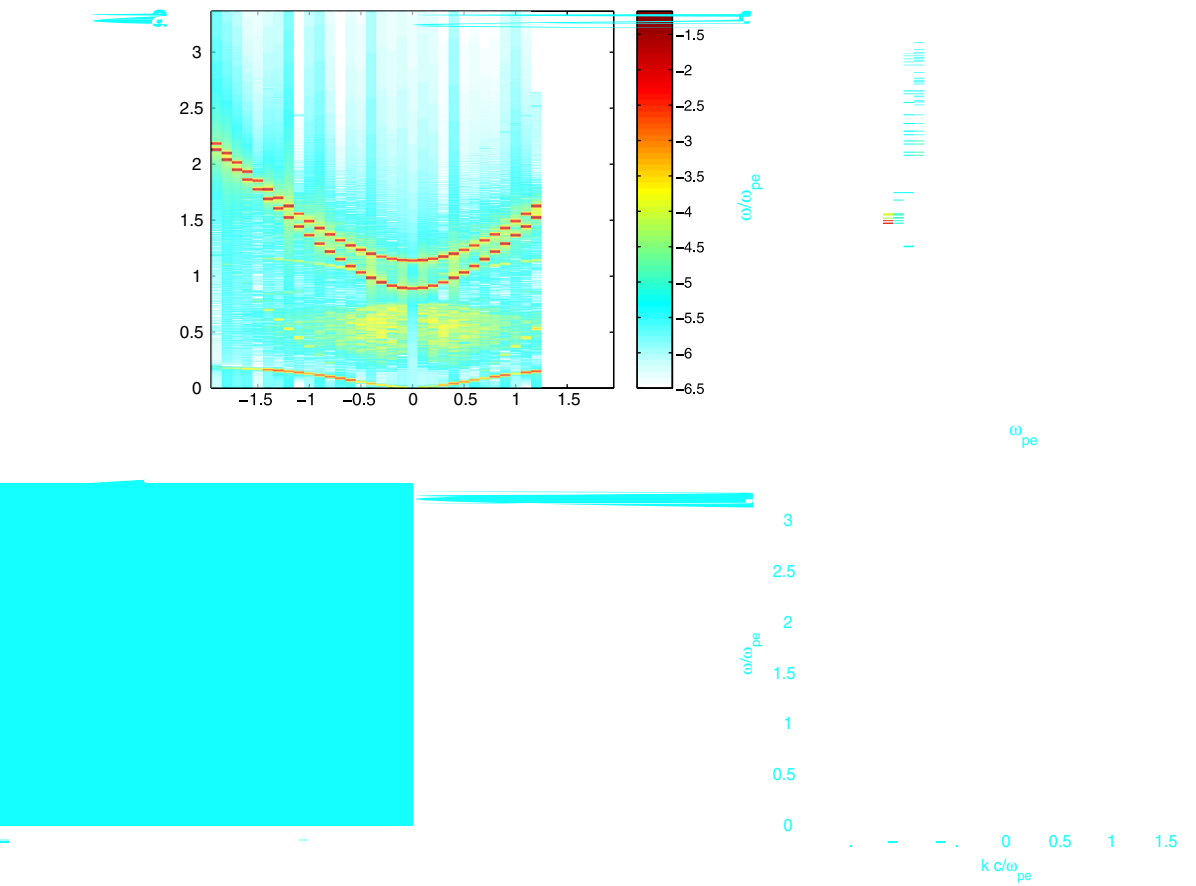

Fig. 2. (a) Amplitude spectrum (10-log scale) of E_2 for waves propagating parallel to the external magnetic field ($\theta = 0$). (b) Dispersion relations for the high-frequency R and L waves and the low-frequency whistler wave, propagating along the external magnetic field ($\theta = 0$). (c) Amplitude spectrum of E_2 for waves propagating with an angle $\theta = \pi/4$ to the external magnetic field, and (d) dispersion relations for electron waves propagating with an angle of $\theta = \pi/4$ to the external magnetic field. Here $\omega_{ce}/\omega_{pe} = 1/4$.

to $20\pi c/\omega_{pe}$ in dimensional units), $N_{\eta_1} = N_{\eta_2} = N_{\eta_3} = 20$, $\eta_{e1,max} = \eta_{e2,max} = \eta_{e3,max} = 6$, and $\eta_{i1,max} = \eta_{i2,max} = \eta_{i3,max} = 200$. The simulations were run with 8000 time-steps with the fixed time interval $\Delta t = 0.14$. In Figs. 2 and 3, we have Fourier transformed the electric field in space and time (with a Gaussian time window) to obtain the spatio-temporal wave spectrum. In panel (a) of Fig. 2, we show the power spectrum for the transversal electric field component E_2, for waves propagating along the magnetic field lines. It is clearly seen that the wave energy is concentrated along the dispersion curves of the electromagnetic right-hand (R) and left-hand (L) circularly polarized waves, shown in in panel (b). They are given by the dispersion relation

$$\frac{c^2k^2}{\omega^2} = 1 - \frac{\omega_{pe}^2/\omega^2}{1 - \omega_{ce}/\omega} \tag{117}$$

and

$$\frac{c^2k^2}{\omega^2} = 1 - \frac{\omega_{pe}^2/\omega^2}{1 + \omega_{ce}/\omega} \tag{118}$$

respectively, obtained by setting $\theta = 0$ in Eq. (114). The R-wave is divided into a high-frequency branch (having the highest frequency) and the low-frequency electron whistler branch. We next made a simulation of waves propagating obliquely to the external magnetic field, which was chosen as $(B_{01}, B_{02}, B_{03}) = (0.25, 0.25, 0)/\sqrt{2}$. The resulting amplitude spectrum of E_2 is presented in panel (c) of Fig. 2, while the solu-

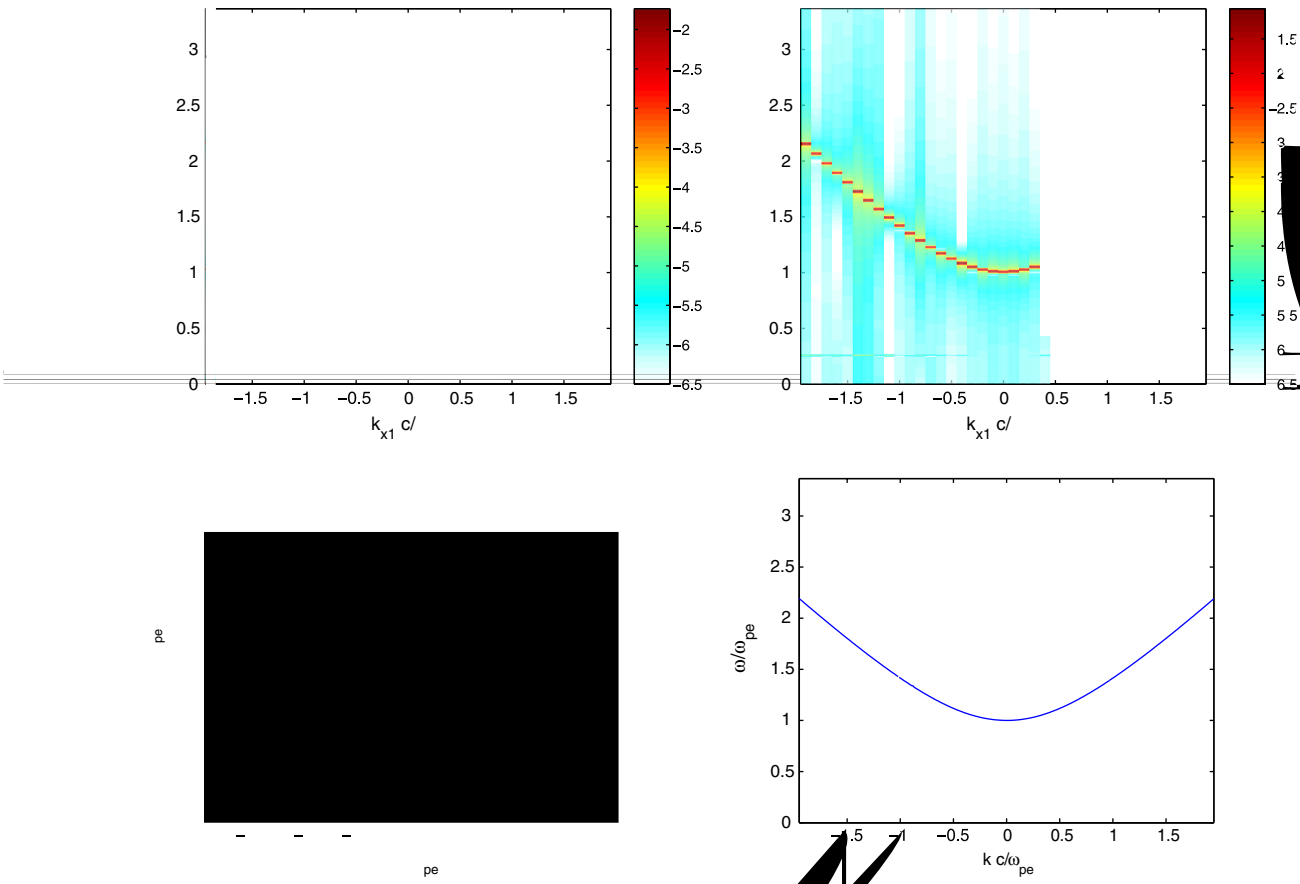

tions of the dispersion relation (114) is pl in panel (d). Here, we can see the appearence of the slow X-mode which has a resonance frequenc ewhat higher than the plasma frequency ω_{pe}. Comparing panel (c) and (d), we see that the wave ener concentrated at the dispersion curves. In Fig. 3, we are considering waves propagating perpendicularl the magnetic field. Here, the external magnetic field is given by $(B_{01}, B_{02}, B_{03}) = (0, 0.25, 0)$, and t nergy spectrum in panel (a) and (c) are for the perpendicular (to the magnetic field direction) and l electric field components E_3 and E_2, respectively. The wave energy is concentrated at the dispers curves for the cold plasma fast and slow X-modes displayed in panel (b) and the O-mode plotted anel (d). The cold plasma dispersion relation for the ordinary (O-) mode and extraordinary (X-) mo perpendicular to the magnetic field, is given by

$$\frac{c^2k^2}{\omega^2} = 1 - \frac{\omega^2}{} \tag{119}$$

and

$$\frac{c^2k^2}{\omega^2} = 1 - \frac{\omega_{pe}^2}{\omega^2}\frac{(\omega^2 - \omega_{pe}^2)}{(\omega^2 - \omega_{pe}^2 - \omega_{ce}^2)}, \tag{120}$$

respectively, obtained by setting $\theta = \pi/2$ in Eq. (114). Also seen in panel (a) at $\omega/\omega_{pe} = 0.5$ is an excitation of an electron Bernstein mode which starts at $\omega = 2\omega_{ce}$ at small wavenumbers and has a resonance at $\omega = \omega_{ce}$ for large wavenumbers.

4.3. Temperature anisotropy driven whistler instability

In magnetized plasmas, there are often different temperatures parallel and perpendicular to the magnetic field direction. In this case, we may have a firehose instability if $T_{e\|} > T_{e\perp}$, or a whistler instability if $T_{e\perp} > T_{e\|}$. The latter case can have relevance both for the sun and for the Earth's magnetosheath [25,26]. In order to study the growth and saturation of the whistler instability, we carried out a simulation where the initial condition for the electrons was taken to be a bi-Maxwellian distribution function, where we used the temperature ratio $T_{e\perp}/T_{e\|} = 8$. In the Fourier transformed velocity variables used in the simulation, the electron and ion distribution function takes the form

$$\hat{f}_e = (2\pi)^{-3} \exp\left[-\frac{(\eta_1^2 + 8\eta_2^2 + 8\eta_3^2)}{2}\right], \tag{121}$$

while for the ions we used

$$\hat{f}_i = (2\pi)^{-3} \exp\left[-\frac{(\eta_1^2 + \eta_2^2 + \eta_3^2)}{2}\left(\frac{T_i m_e}{T_e m_i}\right)^{1/2}\right], \tag{122}$$

with $T_i/T_{e\|} = 100$ and $m_i/m_e = 1836$. We use the same numerical parameters as in Section 4.2, except that $\eta_{e2,max} = \eta_{e3,max} = 3$ and we use a higher resolution in space such that $N_{x1} = 80$. We used an adaptive time step in the simulation with $\alpha = 0.9$ (cf. Section 3.3). The numerical results are displayed in Figs. 4–6. The time-dependence of the maximum amplitude (over the spatial domain) of the perpendicular electric and magnetic field components E_2 and B_2 are shown in Fig. 4, and we see an exponential growth of the perpendicular electric field component E_2, with a growth rate of $\omega_I \approx 0.017\omega_{pe}$ [indicated by the solid line in panel (a)] of both the electric and magnetic field. The initially almost purely electromagnetic waves saturate nonlinearly by exciting the electrostatic field component E_1 (see the upper panel of Fig. 4), and the amplitude of the perpendicular magnetic field fluctuations are at this point about 10% of the external magnetic field. In order to compare the simulation result with theory, we have plotted the spatio-temporal amplitude spectrum of the perpendicular electric field component E_2 in panel (a) of Fig. 5 (in a 10-log scale) where the Fourier transform in time

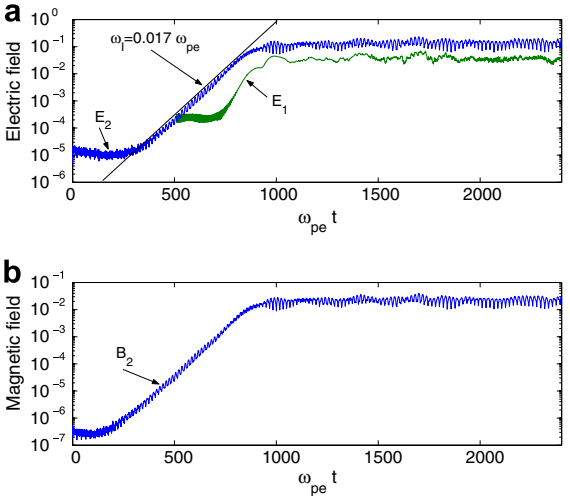

Fig. 4. (a) The maximum amplitude of the parallel and perpendicular electric field components E_1 and E_2, respectively, and (b) the perpendicular magnetic field component B_2. (The parallel electric field E_1 is shown only for times $t > 500\omega_{pe}^{-1}$.) The electric and magnetic fields are normalized according to (30)–(34).

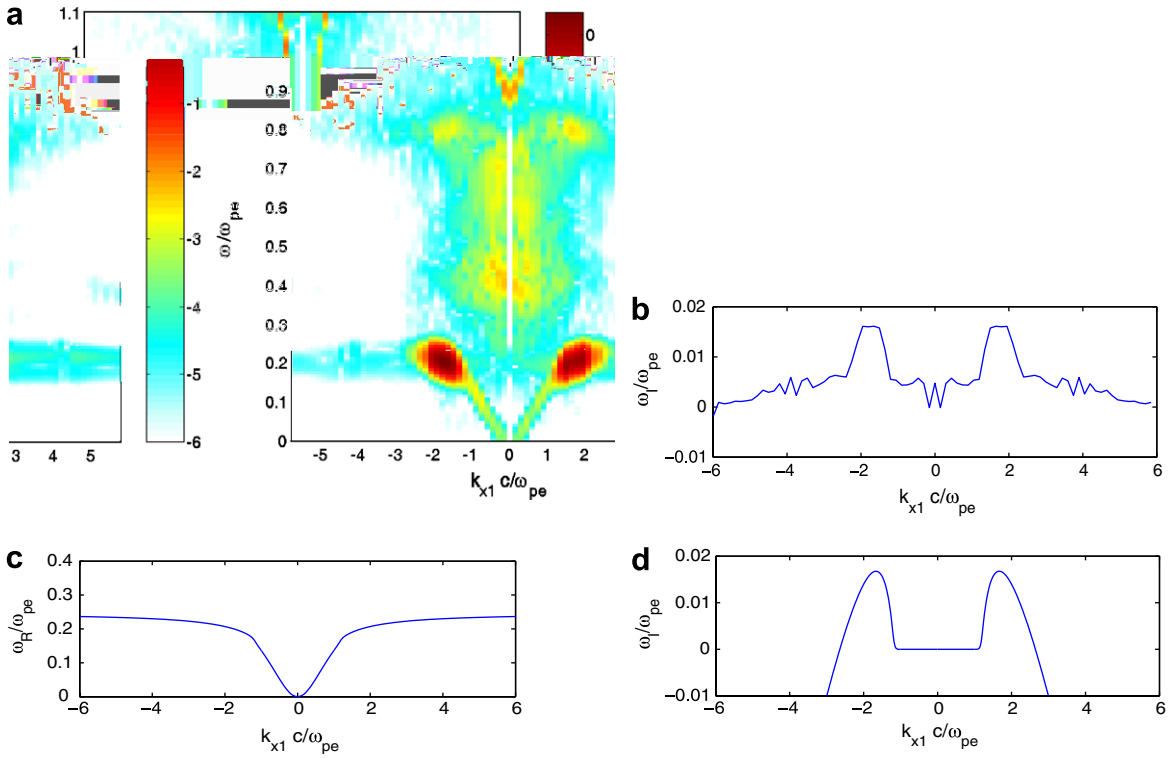

Fig. 5. (a) The spatio-temporal amplitude spectrum of the electric field component E_2, and (b) the spatial amplitude spectrum at time $t = 700\omega_{pe}$. (c) The real and (d) imaginary parts of the frequency for whistler waves, obtained from the dispersion relation (123), in an anisotropic plasma with $T_\perp/T_\parallel = 8$, $c/v_{Te\parallel} = 50$ and $\omega_{ce}/\omega_{pe} = 0.25$.

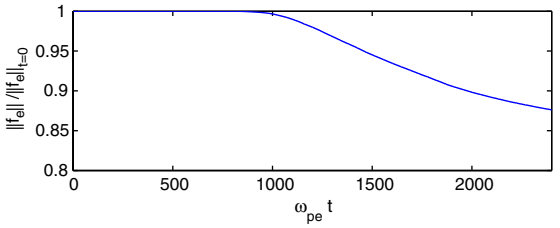

Fig. 6. The energy norm for the electron distribution function, normalized by it initial value. The solution was advanced in time with 20000 time steps.

was taken for waves between $\omega_{pe}t = 0$ and $\omega_{pe}t = 600$, with a Gaussian time window. In panel (b), we have plotted the quantity $\omega_I = (1/t_1)\ln[|\widehat{E}_2(t_1)|] + \text{constant}$ where $\widehat{E}_2$ is the spatial Fourier transform of the electric field component E_2 at time $t = t_1$ and $t_1 = 700\omega_{pe}^{-1}$. Panel (b) gives a rough estimate of the growth rate for different wavenumbers in the simulation. We see that there is a significant growth rate of waves with wavenumbers between $kc/\omega_{pe} \approx 1.2$ and $kc/\omega_{pe} \approx 2.6$. We have solved the dispersion relation for whistler waves in a plasma with a bi-Maxwellian electron distribution. In the one-dimensional case, and for immobile ions, it is [24]

$$\frac{k_\parallel^2 c^2}{\omega_{pe}^2} = \frac{T_{e\perp}}{T_{e\parallel}} - 1 + \frac{(\omega - \omega_{ce})T_{e\perp}/T_{e\parallel} + \omega_{ce}}{\sqrt{2}k_\parallel v_{Te\parallel}} Z\left(\frac{\omega - \omega_{ce}}{\sqrt{2}k_\parallel v_{Te\parallel}}\right), \tag{123}$$

where $v_{Te\parallel} = (k_B T_{e\parallel}/m_e)^{1/2}$ is the parallel electron thermal speed and

$$Z(\xi) = i\sqrt{\pi}\exp(-\xi^2)[1 + \mathrm{erf}(i\xi)] \tag{124}$$

is the plasma dispersion function. In the dispersion relation (123), we have neglected the electromagnetic displacement current term [corresponding to the first term in the right-hand side of Eq. (117)]. In panels (c) and (d) of Fig. 5, we have plotted the real and imaginary parts of the frequency, obtained from the dispersion relation (123), where we have used the simulation parameters $\omega_{ce}/\omega_{pe} = 0.25$, $T_{e\perp}/T_{e\parallel} = 8$ and $c/v_{Te\parallel} = 50$. Comparing panels (a) and (c), we see that for the undamped waves at small wavenumbers, the wave energy of the waves in the simulation is located along the dispersion curve of the whistler wave. Panels (b) and (d) show that the spectrum of the growing waves matches approximately the waves with positive growth rate obtained from the dispersion relation (123). We note that the maximum growth rate $\omega_I \approx 0.017\omega_{pe}$ in panel (d) of Fig. 5 agrees well with the measured growth rate in panel (a) of Fig. 4.

The energy norm for the electron distribution function is shown in Fig. 6. It is decreasing monotonically according to theory and does not show any sign of numerical instability in the simulation. Hence, the numerical scheme seems to be robust also when large-amplitude magnetic and electric fields fluctuate both in space and time.

4.4. The conserved quantities

4.4.1. The number of particles

The numerical scheme conserves globally the number of particles (27) exactly, where the sum representation

$$N_\alpha = (2\pi)^3 \sum_{i_1=0}^{N_{x_1}-1} \sum_{i_2=0}^{N_{x_2}-1} \sum_{i_3=0}^{N_{x_3}-1} \hat{f}_{\alpha,i_1,i_2,i_3,0,0,0} \Delta x_3 \Delta x_2 \Delta x_1 \tag{125}$$

is used to approximate the integrals in (27). The distribution function $\hat{f}$ is evaluated at $\boldsymbol{\eta} = \mathbf{0}$, where the Vlasov equation (70) reduces to

$$\left(\frac{\partial \hat{f}_\alpha}{\partial t}\right)_{\boldsymbol{\eta}=0} - (\mathrm{i}\nabla_{\mathbf{x}} \cdot \nabla_{\boldsymbol{\eta}} \hat{f}_\alpha)_{\boldsymbol{\eta}=0} = 0. \tag{126}$$

By the definitions of the particle number density (20) and mean velocity (21), Eq. (126) expresses the continuity equation on conservative form,

$$\frac{\partial n_\alpha}{\partial t} + \nabla_{\mathbf{x}} \cdot (n_\alpha \mathbf{v}_a) = 0. \tag{127}$$

Hence, where $\boldsymbol{\eta} = 0$, the numerical scheme solves Eq. (127) numerically, where a pseudo-spectral method is used to approximate the spatial derivatives. The periodic boundary conditions leads to a global conservation of the number of particles, which has been verified in the numerical experiments presented in this article.

4.4.2. The total linear momentum and energy

In the scaled variables used, the expressions for the total linear momentum (28) and energy (29) attain the form

$$\mathbf{p}_{\mathrm{tot}} = \int_{\Omega_{\mathbf{x}}} \left[-\mathrm{i}(2\pi)^3 \nabla_{\boldsymbol{\eta}} \left(\frac{m_i}{m_e} \hat{f}_i + \hat{f}_e \right)_{\boldsymbol{\eta}=0} + \mathbf{E} \times \mathbf{B} \right] \mathrm{d}\Omega_{\mathbf{x}} \equiv \mathbf{p}_{\mathrm{matter}} + \mathbf{p}_{\mathrm{EM}}, \tag{128}$$

where $\mathbf{p}_{\mathrm{matter}}$ and $\mathbf{p}_{\mathrm{EM}}$ are the contribution to the linear momentum from the particles and electromagnetic field, respectively, and

$$W_{\mathrm{tot}} = \int_{\Omega_{\mathbf{x}}} \left\{ -\frac{1}{2}(2\pi)^3 \nabla_\eta^2 \left(\frac{m_i}{m_e} \hat{f}_i + \hat{f}_e \right)_{\boldsymbol{\eta}=0} + \frac{1}{2} \left[\mathbf{E}^2 + \frac{c^2}{v_{Te}^2} \mathbf{B}^2 \right] \right\} \mathrm{d}\Omega_{\mathbf{x}} \equiv W_k + W_E + W_B, \tag{129}$$

respectively, where W_k, W_E and W_B is the kinetic, electric and magnetic energy, respectively. The integrals are taken over the rectangular domain in (x_1, x_2, x_3) space, approximated numerically with sum representations. The gradient operator $\nabla_{\boldsymbol{\eta}} = \hat{\mathbf{x}}_1 \partial/\partial\eta_1 + \hat{\mathbf{x}}_2 \partial/\partial\eta_2 + \hat{\mathbf{x}}_3 \partial/\partial\eta_3$ and Laplace operator $\nabla_\eta^2 = \partial^2/\partial\eta_1^2 + \partial^2/\partial\eta_2^2 + \partial^2/\partial\eta_3^2$ are approximated numerically with centered sixth-order difference approximations [27].

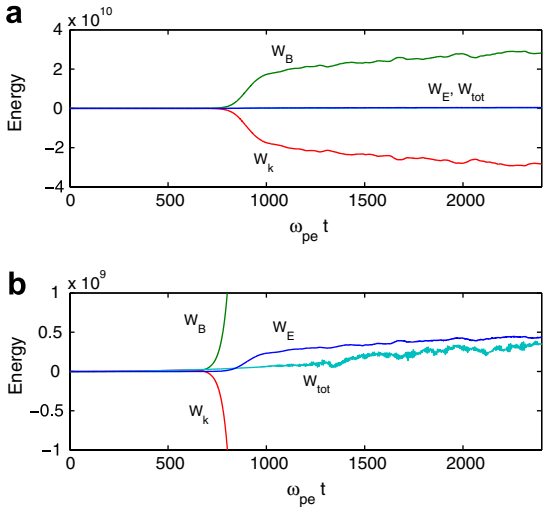

Fig. 7. The time development of the kinetic energy W_k, the electric energy W_E, the magnetic energy W_B, and the total energy $W_{tot} = W_k + W_E + W_B$. Panel (b) is a closeup of panel (a) for small energies.

As a numerical example, we use the simulation of the whistler instability in Section 4.3. In the nonlinear saturation of the whistler instability, most wave energy is cascaded into slightly smaller wavenumbers (larger length scales) than those of the linearly unstable waves, while part of the energy is also cascaded to larger wavenumbers (smaller length scales). It is therefore important to have a dense enough grid in space in order to avoid unphysical folding of waves as they reach the highest represented wavenumber $\pi/\Delta x_1$ in the simulation. In Fig. 7, the time-development of the kinetic, electric and magnetic energy is plotted together with the total energy. We see a significant decrease of the kinetic energy and a corresponding increase of the magnetic energy in the growing whistler waves, while the electric energy fluctuations are comparatively small. We see that amplitude of the fluctuations in the total energy is about one percent of the ones of the kinetic and magnetic energy fluctuations. Numerical tests with smaller number of points N_{x_1} in space have shown that the conservation of energy, and hence the numerical accuracy, quickly deteriorates for lower resolution in x_1 space (for smaller N_{x_1}), due to nonlinear folding of the solution in wavenumber space.

5. Conclusions

A numerical algorithm has been presented, which solves the three-dimensional Vlasov–Maxwell system of equations numerically. The algorithm is based on a Fourier transform technique in which the Vlasov equation is Fourier transformed analytically in velocity space and the resulting equations are solved numerically. In order to reduce numerical recurrence effects due to the phase-mixing in velocity space, well-posed absorbing boundary conditions have been designed in the Fourier transformed velocity space. The stability of the implemented algorithm has been assessed by long-time numerical runs with random data/noise as initial conditions. It has been shown that the numerical code reproduces well-known plasma waves in a magnetized plasma, as well as a well-known electron whistler instability due to a temperature anisotropy. In order to be able to use the algorithm on realistic problems in multiple dimensions, it will be necessary to parallelize the code in the future. For that purpose the parallelized one-dimensional Vlasov code [23] may serve as a prototype.

Acknowledgements

This research was financially supported by Swedish Research Council (VR) as well as by the Deutsche Forschungsgemeinschaft through the Sonderforschungsbereich 591. The author wishes to acknowledge the Swedish High Performance Computing Center North (HPC2N) for the provision of computational facilities and support.

Appendix A. Proof of the well-posedness of the absorbing boundary conditions

In the present Appendix, a proof is given of the well-posedness of the Fourier transformed Vlasov equation (42) restricted to a bounded domain and with the boundary conditions given in Section 2.4. We will use the short notation for the integral expressions,

$$\int_{\mathbf{x}} \mathrm{d}^3x \equiv \int_{x_1=0}^{L_1}\int_{x_2=0}^{L_2}\int_{x_3=0}^{L_3} \mathrm{d}x_3\mathrm{d}x_2\mathrm{d}x_1 \tag{A.1}$$

and

$$\int_{\boldsymbol{\eta}} \mathrm{d}^3\eta \equiv \int_{\eta_1=0}^{\eta_{\alpha 1,\max}}\int_{\eta_2=-\eta_{\alpha 2,\max}}^{\eta_{\alpha 2,\max}}\int_{\eta_3=-\eta_{\alpha 3,\max}}^{\eta_{\alpha 3,\max}} \mathrm{d}\eta_3\mathrm{d}\eta_2\mathrm{d}\eta_1, \tag{A.2}$$

when convenient.

The problem is well-posed if the squared energy norm

$$\|\hat{f}_\alpha\|^2 = \int_{\mathbf{x}}\int_{\boldsymbol{\eta}} |\hat{f}_\alpha|^2 \mathrm{d}^3\eta\mathrm{d}^3x = \int_{\mathbf{x}}\int_{\boldsymbol{\eta}} \hat{f}_\alpha \hat{f}^*_\alpha \mathrm{d}^3\eta\mathrm{d}^3x \tag{A.3}$$

is bounded for all times [22]. (The asterisk denotes complex conjugation.) In the following, we prove that the squared norm (A.3) is non-increasing with time. Taking the time derivative of the squared norm,

$$\frac{\mathrm{d}\|\hat{f}_\alpha\|^2}{\mathrm{d}t} = \int_{\mathbf{x}}\int_{\boldsymbol{\eta}} \left(\hat{f}^*_\alpha \frac{\partial \hat{f}_\alpha}{\partial t} + \hat{f}_\alpha \frac{\partial \hat{f}^*_\alpha}{\partial t}\right)\mathrm{d}^3\eta\mathrm{d}^3x \tag{A.4}$$

and then replacing the time derivatives with the help of Eq. (70) gives

$$\begin{aligned}
\frac{\mathrm{d}\|\hat{f}_\alpha\|^2}{\mathrm{d}t} = \int_{\mathbf{x}}\int_{\boldsymbol{\eta}} \Bigg(& -\hat{f}^*_\alpha \Bigg\{ \exp\left[\mathrm{i}\int_0^{x_1}(\beta_1-\beta_{01})\mathrm{d}x_1\right]\frac{\partial}{\partial\eta_1}\left(-\mathrm{i}\frac{\partial}{\partial x_1}-\beta_{01}\right)G_{\alpha 1}. + \exp\left[\mathrm{i}\int_0^{x_2}(\beta_2-\beta_{02})\mathrm{d}x_2\right]\frac{\partial}{\partial\eta_2} \\
& \times\left(-\mathrm{i}\frac{\partial}{\partial x_2}-\beta_{02}\right)G_{\alpha 2} + \exp\left[\mathrm{i}\int_0^{x_3}(\beta_3-\beta_{03})\mathrm{d}x_3\right]\frac{\partial}{\partial\eta_3}\left(-\mathrm{i}\frac{\partial}{\partial x_3}-\beta_{03}\right)G_{\alpha 3} + \mathrm{i}(\eta_1E_1+\eta_2E_2+\eta_3E_3)\hat{f}_\alpha \Bigg\} \\
& -\hat{f}_\alpha \Bigg\{ \exp\left[-\mathrm{i}\int_0^{x_1}(\beta_1-\beta_{01})\mathrm{d}x_1\right]\frac{\partial}{\partial\eta_1}\left(\mathrm{i}\frac{\partial}{\partial x_1}-\beta_{01}\right)G^*_{\alpha 1} + \exp\left[-\mathrm{i}\int_0^{x_2}(\beta_2-\beta_{02})\mathrm{d}x_2\right]\frac{\partial}{\partial\eta_2}\left(\mathrm{i}\frac{\partial}{\partial x_2}-\beta_{02}\right)G^*_{\alpha 2}. \\
& + \exp\left[-\mathrm{i}\int_0^{x_3}(\beta_3-\beta_{03})\mathrm{d}x_3\right]\frac{\partial}{\partial\eta_3}\left(\mathrm{i}\frac{\partial}{\partial x_3}-\beta_{03}\right)G^*_{\alpha 3} - \mathrm{i}(\eta_1E_1+\eta_2E_2+\eta_3E_3)\hat{f}^*_\alpha \Bigg\}\Bigg)\mathrm{d}^3\eta\mathrm{d}^3x
\end{aligned} \tag{A.5}$$

where the terms containing E_1, E_2 and E_3 cancel out. Using the definitions (71)–(73) for $G_{\alpha 1}$, $G_{\alpha 2}$ and $G_{\alpha 3}$, we have

$$\begin{aligned}
\frac{\mathrm{d}\|\hat{f}_\alpha\|^2}{\mathrm{d}t} = & \int_{\mathbf{x}}\int_{\boldsymbol{\eta}} \Bigg[-G^*_{\alpha 1}\frac{\partial}{\partial\eta_1}\left(-\mathrm{i}\frac{\partial}{\partial x_1}-\beta_{01}\right)G_{\alpha 1} - G^*_{\alpha 2}\frac{\partial}{\partial\eta_2}\left(-\mathrm{i}\frac{\partial}{\partial x_2}-\beta_{02}\right)G_{\alpha 2} - G^*_{\alpha 3}\frac{\partial}{\partial\eta_3}\left(-\mathrm{i}\frac{\partial}{\partial x_3}-\beta_{03}\right)G_{\alpha 3} \\
& - G_{\alpha 1}\frac{\partial}{\partial\eta_1}\left(\mathrm{i}\frac{\partial}{\partial x_1}-\beta_{01}\right)G^*_{\alpha 1} - G_{\alpha 2}\frac{\partial}{\partial\eta_2}\left(\mathrm{i}\frac{\partial}{\partial x_2}-\beta_{02}\right)G^*_{\alpha 2} - G_{\alpha 3}\frac{\partial}{\partial\eta_3}\left(\mathrm{i}\frac{\partial}{\partial x_3}-\beta_{03}\right)G^*_{\alpha 3}\Bigg]\mathrm{d}^3\eta\mathrm{d}^3x \\
& \times\int_{\mathbf{x}}\int_{\boldsymbol{\eta}} \Bigg[\mathrm{i}\frac{\partial}{\partial\eta_1}\left(G^*_{\alpha 1}\frac{\partial G_{\alpha 1}}{\partial x_1}\right) - \mathrm{i}\frac{\partial}{\partial x_1}\left(G_{\alpha 1}\frac{\partial G^*_{\alpha 1}}{\partial\eta_1}\right) + \mathrm{i}\frac{\partial}{\partial\eta_2}\left(G^*_{\alpha 2}\frac{\partial G_{\alpha 2}}{\partial x_2}\right) - \mathrm{i}\frac{\partial}{\partial x_2}\left(G_{\alpha 2}\frac{\partial G^*_{\alpha 2}}{\partial\eta_2}\right) \\
& + \mathrm{i}\frac{\partial}{\partial\eta_3}\left(G^*_{\alpha 3}\frac{\partial G_{\alpha 3}}{\partial x_3}\right) - \mathrm{i}\frac{\partial}{\partial x_3}\left(G_{\alpha 3}\frac{\partial G^*_{\alpha 3}}{\partial\eta_3}\right) + \beta_{01}\frac{\partial}{\partial\eta_1}(G_{\alpha 1}G^*_{\alpha 1}) + \beta_{02}\frac{\partial}{\partial\eta_2}(G_{\alpha 2}G^*_{\alpha 2}) + \beta_{03}\frac{\partial}{\partial\eta_3}(G_{\alpha 3}G^*_{\alpha 3})\Bigg]\mathrm{d}^3\eta\mathrm{d}^3x
\end{aligned} \tag{A.6}$$

which can be integrated one step,

$$\begin{aligned}\frac{\mathrm{d}\|\hat{f}_\alpha\|^2}{\mathrm{d}t} = &\int_{\mathbf{x}} \int_{\eta_2=-\eta_{\alpha 2,\max}}^{\eta_{\alpha 2,\max}} \int_{\eta_3=-\eta_{\alpha 3,\max}}^{\eta_{\alpha 3,\max}} \left[\mathrm{i} G^*_{\alpha 1} \frac{\partial G_{\alpha 1}}{\partial x_1} + \beta_{01} G^*_{\alpha 1} G_{\alpha 1} \right]_{\eta_1=0}^{\eta_{\alpha 1,\max}} \mathrm{d}\eta_3 \mathrm{d}\eta_2 \mathrm{d}^3 x \\ &+ \int_{\mathbf{x}} \int_{\eta_1=0}^{\eta_{\alpha 1,\max}} \int_{\eta_3=-\eta_{\alpha 3,\max}}^{\eta_{\alpha 3,\max}} \left[\mathrm{i} G^*_{\alpha 2} \frac{\partial G_{\alpha 2}}{\partial x_2} + \beta_{02} G^*_{\alpha 2} G_{\alpha 2} \right]_{\eta_2=-\eta_{\alpha 2,\max}}^{\eta_{\alpha 2,\max}} \mathrm{d}\eta_3 \mathrm{d}\eta_1 \mathrm{d}^3 x \\ &+ \int_{\mathbf{x}} \int_{\eta_1=0}^{\eta_{\alpha 1,\max}} \int_{\eta_2=-\eta_{\alpha 2,\max}}^{\eta_{\alpha 2,\max}} \left[\mathrm{i} G^*_{3} \frac{\partial G_{3}}{\partial x_3} + \beta_{03} G^*_{\alpha 3} G_{\alpha 3} \right]_{\eta_3=-\eta_{\alpha 3,\max}}^{\eta_{\alpha 3,\max}} \mathrm{d}\eta_2 \mathrm{d}\eta_1 \mathrm{d}^3 x \\ &- \int_{x_2=0}^{L_2} \int_{x_3=0}^{L_3} \int_{\boldsymbol{\eta}} \left[\mathrm{i} G_{\alpha 1} \frac{\partial G^*_{\alpha 1}}{\partial \eta_1} \right]_{x_1=0}^{L_1} \mathrm{d}^3\eta \mathrm{d}x_3 \mathrm{d}x_2 - \int_{x_1=0}^{L_1} \int_{x_3=0}^{L_3} \int_{\boldsymbol{\eta}} \left[\mathrm{i} G_{\alpha 2} \frac{\partial G^*_{\alpha 2}}{\partial \eta_2} \right]_{x_2=0}^{L_2} \mathrm{d}^3\eta \mathrm{d}x_3, \mathrm{d}x_1 \\ &- \int_{x_1=0}^{L_1} \int_{x_2=0}^{L_2} \int_{\boldsymbol{\eta}} \left[\mathrm{i} G_{\alpha 3} \frac{\partial G^*_{\alpha 3}}{\partial \eta_3} \right]_{x_3=0}^{L_3} \mathrm{d}^3\eta \mathrm{d}x_2, \mathrm{d}x_1, \end{aligned} \tag{A.7}$$

where the last three terms vanish due to periodic boundary conditions in the x_1, x_2 and x_x directions.

The first integral in Eq. (A.7) vanishes at the limit $\eta_1 = 0$, due to symmetry: The function $G_{\alpha 1}$ obeys the same symmetry properties (19) as $\hat{f}_\alpha$, which is easily seen from the definition (71) of $G_{\alpha 1}$. Therefore the product $G_{\alpha 1} G^*_{\alpha 1}$ is an *even* function with respect to (η_2, η_3) at $\eta_1 = 0$, and the expression $\beta_{01} G_{\alpha 1} G^*_{\alpha 1}$ is an *odd* function with respect to (η_2, η_3). The integral of the second term $\beta_{01} G_{\alpha 1} G^*_{\alpha 1}$ over the even intervals $-\eta_{\alpha 2,\max} \leqslant \eta_2 \leqslant \eta_{\alpha 2,\max}$ and $-\eta_{\alpha 3,\max} \leqslant \eta_3 \leqslant \eta_{\alpha 3,\max}$ therefore vanishes. The first term in the integral vanishes because of the symmetry (19) and the periodic boundary conditions in x_1 direction, as is shown here:

$$\int_{\mathbf{x}} \int_{\eta_2=-\eta_{\alpha 2,\max}}^{\eta_{\alpha 2,\max}} \int_{\eta_3=-\eta_{\alpha 3,\max}}^{\eta_{\alpha 3,\max}} \left[G^*_{\alpha 1} \frac{\partial G_{\alpha 1}}{\partial x_1} \right]_{\eta_1=0} \mathrm{d}\eta_3 \mathrm{d}\eta_2 \mathrm{d}^3 x = \int_{\mathbf{x}} \int_{\eta_2=\eta_{\alpha 2,\max}}^{-\eta_{\alpha 2,\max}} \int_{\eta_3=\eta_{\alpha 3,\max}}^{-\eta_{\alpha 3,\max}} \left[G^*_{\alpha 1} \frac{\partial G_{\alpha 1}}{\partial x_1} \right]_{\eta_1=0} \mathrm{d}\eta_3 \mathrm{d}\eta_2 \mathrm{d}^3 x$$

[Change variables η_2 to $-\eta_2$ and η_3 to $-\eta_3$]

$$= \int_{\mathbf{x}} \int_{\eta_2=-\eta_{\alpha 2,\max}}^{\eta_{\alpha 2,\max}} \int_{\eta_3=-\eta_{\alpha 3,\max}}^{\eta_{\alpha 3,\max}} \left[G^*_{\alpha 1}(x_1, x_2, x_3, 0, -\eta_2, -\eta_3, t) \frac{\partial}{\partial x_1} G_{\alpha 1}(x_1, x_2, x_3, 0, -\eta_2, -\eta_3, t) \right] \mathrm{d}\eta_3 \mathrm{d}\eta_2 \mathrm{d}^3 x$$

[Use the symmetry (19)]

$$= \int_{\mathbf{x}} \int_{\eta_2=-\eta_{\alpha 2,\max}}^{\eta_{\alpha 2,\max}} \int_{\eta_3=-\eta_{\alpha 3,\max}}^{\eta_{\alpha 3,\max}} \left[G_{\alpha 1}(x_1, x_2, x_3, 0, \eta_2, \eta_3, t) \frac{\partial}{\partial x_1} G^*_{\alpha 1}(x_1, x_2, x_3, 0, \eta_2, \eta_3, t) \right] \mathrm{d}\eta_3 \mathrm{d}\eta_2 \mathrm{d}^3 x$$

[Integrate by parts in x_1 direction]

$$\begin{aligned} &= \int_{x_2=0}^{L_2} \int_{x_3=0}^{L_3} \int_{\eta_2=-\eta_{\alpha 2,\max}}^{\eta_{\alpha 2,\max}} \int_{\eta_3=-\eta_{\alpha 3,\max}}^{\eta_{\alpha 3,\max}} \left[\left(G_{\alpha 1} G^*_{\alpha 1} \right)_{x_1=0}^{L_1} - \int_{x_1=0}^{L_1} G^*_{\alpha 1} \frac{\partial G_{\alpha 1}}{\partial x_1} \mathrm{d}x_1 \right]_{\eta_1=0} \mathrm{d}\eta_3 \mathrm{d}\eta_2 \mathrm{d}x_3 \mathrm{d}x_2 \\ &= - \int_{\mathbf{x}} \int_{\eta_2=-\eta_{\alpha 2,\max}}^{\eta_{\alpha 2,\max}} \int_{\eta_3=-\eta_{\alpha 3,\max}}^{\eta_{\alpha 3,\max}} \left[G^*_{\alpha 1} \frac{\partial G_{\alpha 1}}{\partial x_1} \right]_{\eta_1=0} \mathrm{d}\eta_3 \mathrm{d}\eta_2 \mathrm{d}^3 x. \end{aligned} \tag{A.8}$$

The same expression appears on the left-hand side and right-hand side with opposite signs; thus the expression must be equal to zero.

What remains of Eq. (A.7), after reordering of the terms, is

$$\begin{aligned}\frac{\mathrm{d}\|\hat{f}_\alpha\|^2}{\mathrm{d}t} = &\int_{x_2=0}^{L_2} \int_{x_3=0}^{L_3} \int_{\eta_2=-\eta_{\alpha 2,\max}}^{\eta_{\alpha 2,\max}} \int_{\eta_2=-\eta_{\alpha 3,\max}}^{\eta_{\alpha 3,\max}} (R_{\alpha 1})_{\eta_1=\eta_{\alpha 1,\max}} \mathrm{d}\eta_3 \mathrm{d}\eta_2 \mathrm{d}x_3 \mathrm{d}x_2 \\ &+ \int_{x_1=0}^{L_1} \int_{x_3=0}^{L_3} \int_{\eta_1=0}^{\eta_{\alpha 1,\max}} \int_{\eta_3=-\eta_{\alpha 3,\max}}^{\eta_{\alpha 3,\max}} [(R_{\alpha 2})_{\eta_2=\eta_{\alpha 2,\max}} - (R_{\alpha 2})_{\eta_2=-\eta_{\alpha 2,\max}}] \mathrm{d}\eta_3 \mathrm{d}\eta_1 \mathrm{d}x_3 \mathrm{d}x_1 \\ &+ \int_{x_1=0}^{L_1} \int_{x_2=0}^{L_2} \int_{\eta_1=0}^{\eta_{\alpha 1,\max}} \int_{\eta_2=-\eta_{\alpha 2,\max}}^{\eta_{\alpha 2,\max}} [(R_{\alpha 3})_{\eta_3=\eta_{\alpha 3,\max}} - (R_{\alpha 3})_{\eta_3=-\eta_{\alpha 3,\max}}] \mathrm{d}\eta_2 \mathrm{d}\eta_1 \mathrm{d}x_2 \mathrm{d}x_1, \end{aligned} \tag{A.9}$$

where

$$R_{\alpha 1} = \int_{x_1=0}^{L_1} G_{\alpha 1}^* \left(\mathrm{i}\frac{\partial}{\partial x_1} + \beta_{01} \right) G_{\alpha 1} \mathrm{d}x_1, \tag{A.10}$$

$$R_{\alpha 2} = \int_{x_2=0}^{L_2} G_{\alpha 2}^* \left(\mathrm{i}\frac{\partial}{\partial x_2} + \beta_{02} \right) G_{\alpha 2} \mathrm{d}x_2 \tag{A.11}$$

and

$$R_{\alpha 3} = \int_{x_3=0}^{L_3} G_{\alpha 3}^* \left(\mathrm{i}\frac{\partial}{\partial x_3} + \beta_{03} \right) G_{\alpha 3} \mathrm{d}x_3. \tag{A.12}$$

By using the Parseval relation for the Fourier series pairs (48)–(53),

$$\int_{x_1=0}^{L_1} G_{\alpha 1}^* \Gamma_{\alpha 1} \mathrm{d}x_1 = L_1 \sum_{i_1=-\infty}^{\infty} \widetilde{G}_{\alpha 1, i_1}^* \widetilde{\Gamma}_{\alpha 1, i_1} = L_1 \sum_{i_1=-\infty}^{\infty} (\mathrm{F}_1 G_{\alpha 1})_{i_1}^* (\mathrm{F}_1 \Gamma_{\alpha 1})_{i_1}, \tag{A.13}$$

$$\int_{x_2=0}^{L_2} G_{\alpha 2}^* \Gamma_{\alpha 2} \mathrm{d}x_2 = L_2 \sum_{i_2=-\infty}^{\infty} \widetilde{G}_{\alpha 2, i_2}^* \widetilde{\Gamma}_{\alpha 2, i_2} = L_2 \sum_{i_2=-\infty}^{\infty} (\mathrm{F}_2 G_{\alpha 2})_{i_2}^* (\mathrm{F}_2 \Gamma_{\alpha 2})_{i_2}, \tag{A.14}$$

$$\int_{x_3=0}^{L_3} G_{\alpha 3}^* \Gamma_{\alpha 3} \mathrm{d}x_3 = L_3 \sum_{i_3=-\infty}^{\infty} \widetilde{G}_{\alpha 3, i_3}^* \widetilde{\Gamma}_{\alpha 3, i_3} = L_3 \sum_{i_3=-\infty}^{\infty} (\mathrm{F}_3 G_{\alpha 3})_{i_3}^* (\mathrm{F}_3 \Gamma_{\alpha 2})_{i_3}, \tag{A.15}$$

where, from Eqs. (A.10)–(A.12),

$$\Gamma_{\alpha 1} = \left(\mathrm{i}\frac{\partial}{\partial x_1} + \beta_{01} \right) G_{\alpha 1}, \quad \Gamma_{\alpha 2} = \left(\mathrm{i}\frac{\partial}{\partial x_2} + \beta_{02} \right) G_{\alpha 2}, \quad \Gamma_{\alpha 3} = \left(\mathrm{i}\frac{\partial}{\partial x_3} + \beta_{03} \right) G_{\alpha 3}, \tag{A.16}$$

into Eqs. (A.10)–(A.12), we have

$$R_{\alpha 1} = L_1 \sum_{i_1=-\infty}^{\infty} |(\mathrm{F}_1 G_{\alpha 1})_{i_1}|^2 (-k_{x_1} + \beta_{01}), \tag{A.17}$$

$$R_{\alpha 2} = L_2 \sum_{i_2=-\infty}^{\infty} |(\mathrm{F}_2 G_{\alpha 2})_{i_2}|^2 (-k_{x_2} + \beta_{02}), \tag{A.18}$$

$$R_{\alpha 3} = L_3 \sum_{i_3=-\infty}^{\infty} |(\mathrm{F}_3 G_{\alpha 3})_{i_3}|^2 (-k_{x_3} + \beta_{03}), \tag{A.19}$$

where $k_{x_1} = 2\pi i_1/L_1$, $k_{x_2} = 2\pi i_2/L_2$ and $k_{x_3} = 2\pi i_3/L_3$. By applying the boundary conditions (77)–(79) on Eqs. (A.17)–(A.19), we now have

$$(R_{\alpha 1})_{\eta_1 = \eta_{\alpha 1, \max}} = L_1 \sum_{i_1=-\infty}^{\infty} |(\mathrm{F}_1 G_{\alpha 1})_{i_1}|^2 (-k_{x_1} + \beta_{01}) H(k_{x_1} - \beta_{01}), \tag{A.20}$$

$$(R_{\alpha 2})_{\eta_2 = -\eta_{\alpha 2, \max}} = L_2 \sum_{i_2=-\infty}^{\infty} |(\mathrm{F}_2 G_{\alpha 2})_{i_2}|^2 (-k_{x_2} + \beta_{02}) H(-k_{x_2} + \beta_{02}), \tag{A.21}$$

$$(R_{\alpha 2})_{\eta_2 = \eta_{\alpha 2, \max}} = L_2 \sum_{i_2=-\infty}^{\infty} |(\mathrm{F}_2 G_{\alpha 2})_{i_2}|^2 (-k_{x_2} + \beta_{02}) H(k_{x_2} - \beta_{02}), \tag{A.22}$$

$$(R_{\alpha 3})_{\eta_3 = -\eta_{\alpha 3, \max}} = L_3 \sum_{i_3=-\infty}^{\infty} |(\mathrm{F}_3 G_{\alpha 3})_{i_3}|^2 (-k_{x_3} + \beta_{03}) H(-k_{x_3} + \beta_{03}), \tag{A.23}$$

$$(R_{\alpha 3})_{\eta_3 = \eta_{\alpha 3, \max}} = L_3 \sum_{i_3=-\infty}^{\infty} |(\mathrm{F}_3 G_{\alpha 3})_{i_3}|^2 (-k_{x_3} + \beta_{03}) H(k_{x_3} - \beta_{03}), \tag{A.24}$$

and we see that the Heaviside function truncates the sums so that $(R_1)_{\eta_1 = \eta_{\alpha 1, \max}} \leqslant 0$, $(R_2)_{\eta_2 = -\eta_{\alpha 2, \max}} \geqslant 0$, $(R_2)_{\eta_2 = \eta_{\alpha 2, \max}} \leqslant 0$, $(R_3)_{\eta_3 = -\eta_{\alpha 3, \max}} \geqslant 0$ and $(R_3)_{\eta_3 = \eta_{\alpha 3, \max}} \leqslant 0$. Hence every term in the right-hand side of Eq.

(A.9) is non-positive and therefore the energy norm is non-increasing with time. We conclude that the problem with the given boundary conditions is well-posed.

References

[1] C.K. Birdsall, A.B. Langdon, Plasma Physics Via Computer Simulation, Inst of Physics, Bristol, 1991.
[2] H. Matsumoto, Y. Omura, Computer Space Plasma Physics: Simulation Techniques and Software, Terra Scientific Publishing Company, Tokyo, 1993.
[3] T.P. Armstrong, R.C. Harding, G. Knorr, D. Montgomery, Solution of Vlasov's equation by transform methods, Methods in Computational Physics, vol. 9, Academic Press, 1970, pp. 29–86.
[4] C.Z. Cheng, G. Knorr, The integration of the Vlasov equation in configuration space, J. Comput. Phys. 22 (1976) 330–351.
[5] C.Z. Cheng, The integration of the Vlasov equation for a magnetized plasma, J. Comput. Phys. 24 (1977) 348–360.
[6] A. Mangeney, F. Califano, C. Cavazzoni, P. Travnicek, A numerical scheme for the integration of the Vlasov–Maxwell system of equations, J. Comput. Phys. 179 (2002) 495–538.
[7] N.V. Elkina, J. Büchner, J. Comput. Phys. 213 (2006) 862–875.
[8] H. Schmitz, R. Grauer, Comparison of time splitting and backsubstitution methods for integrating Vlasov's equation with magnetic fields, Comput. Phys. Commun. 175 (2006) 86–92.
[9] T.D. Arber, R.G.L. Vann, A Critical Comparison of Eulerian-Grid-Based Vlasov Solvers, J. Comput. Phys. 180 (2002) 339–357.
[10] F. Filbet, E. Sonnendrücker, Comparison of Eulerian Vlasov solvers, Comput. Phys. Commun. 150 (2003) 247–266.
[11] A.J. Klimas, A method for overcoming the velocity space filamentation problem in collisionless plasma model solutions, J. Comput. Phys. 68 (1987) 202–226.
[12] A.J. Klimas, W.M. Farrel, A splitting algorithm for Vlasov simulation with filamentation filtration, J. Comput. Phys. 110 (1994) 150–163.
[13] Z. Sedlacec, L. Nocera, Second-order oscillations of a Vlasov–Poisson plasma in Fourier-transformed velocity space, J. Plasma Phys. 48 (1992) 367–389.
[14] Z. Sedlacec, L. Nocera, Linear Vlasov plasma oscillations in the Fourier transformed velocity space, Phys. lett. A 296 (2002) 117–124.
[15] G. Knorr, M. Shoucri, Plasma simulation as eigenvalue problem, J. Comput. Phys. 14 (1974) 1–7.
[16] L. Gibelli, B.D. Shizgal, Spectral convergence of the Hermite basis function solution of the Vlasov equation: The free-streaming term, J. Comput. Phys. 219 (2006) 477–488.
[17] B. Eliasson, Outflow boundary conditions for the Fourier transformed one-dimensional Vlasov-Poisson system, J. Sci. Comput. 16 (2001) 1–28.
[18] B. Eliasson, Outflow boundary conditions for the Fourier transformed two-dimensional Vlasov equation, J. Comput. Phys. 181 (2002) 98–125.
[19] B. Eliasson, Numerical modelling of the two-dimensional Fourier transformed Vlasov–Maxwell system, J. Comput. Phys. 190 (2003) 501–522.
[20] B. Gustafsson, P. Olsson, Fourth-order difference methods for hyperbolic IBVPs, J. Comput. Phys. 117 (1995) 300–317.
[21] S.K. Lele, Compact finite difference schemes with spectral-like resolution, J. Comput. Phys. 103 (1992) 16–42.
[22] J.C. Strikwerda, Finite Difference Schemes and Partial Differential Equations, Wadsworth & Books, Pacific Grove, CA, 1989 (Chapter 1.6).
[23] B. Eliasson, The parallel implementation of the one-dimensional Fourier transformed Vlasov-Poisson system, Comput. Phys. Commun. 170 (2006) 205–230.
[24] H. Stix, Waves in Plasmas, Springer-Verlag, New York, 1992.
[25] J. Zhao, J.-I. Sakai, K.-I. Nichikawa, Excitation of whistler waves driven by an electron temperature anisotropy, Solar Phys. 168 (1996) 345–355.
[26] J.T. Gosling, M.F. Thomsen, S.J. Bames, C.T. Russell, Suprathermal electrons at Earth's bow shock, J. Geophys. Res. 94 (1989) 10011–10025.
[27] Lennart Råde, Bertil Westergren, BETA Mathematics Handbook, second edition., Studentlitteratur AB, Lund, Sweden, 2002.